Gas phase Elemental abundances in Molecular cloudS (GEMS) I. The prototypical dark cloud TMC 1

D. Navarro, P. Caselli, M. Gerin, C. Krammer, E. Roueff, Valentine Wakelam, T. Alonso-Albi, R. Bachiller, S. Cazaux, B. Commerçon, et al.

A&A 624, A105 (2019)
https://doi.org/10.1051/0004-6361/201834654

Astronomy & Astrophysics

Gas phase Elemental abundances in Molecular cloudS (GEMS)

I. The prototypical dark cloud TMC 1

A. Fuente[1], D. G. Navarro[1], P. Caselli[2], M. Gerin[3], C. Kramer[4], E. Roueff[5], T. Alonso-Albi[1], R. Bachiller[1], S. Cazaux[6,7], B. Commercon[8], R. Friesen[9], S. García-Burillo[1], B. M. Giuliano[2], J. R. Goicoechea[10], P. Gratier[11], A. Hacar[12], I. Jiménez-Serra[13], J. Kirk[14], V. Lattanzi[2], J. C. Loison[15], J. Malinen[16,17], N. Marcelino[10], R. Martín-Doménech[18], G. Muñoz-Caro[13], J. Pineda[2], M. Tafalla[1], B. Tercero[1], D. Ward-Thompson[19], S. P. Treviño-Morales[20], P. Riviére-Marichalar[1], O. Roncero[10], T. Vidal[11], and M. Y. Ballester[21]

[1] Observatorio Astronómico Nacional (OAN), Alfonso XII, 3, 28014 Madrid, Spain
e-mail: a.fuente@oan.es
[2] Centre for Astrochemical Studies, Max-Planck-Institute for Extraterrestrial Physics, Giessenbachstrasse 1, 85748 Garching, Germany
[3] Observatoire de Paris, PSL Research University, CNRS, École Normale Supérieure, Sorbonne Universités, UPMC Université Paris 06, 75005 Paris, France
[4] Instituto Radioastronomía Milimétrica (IRAM), Av. Divina Pastora 7, Nucleo Central, 18012 Granada, Spain
[5] Sorbonne Université, Observatoire de Paris, Université PSL, CNRS, LERMA, 92190 Meudon, France
[6] Faculty of Aerospace Engineering, Delft University of Technology, Delft, The Netherlands
[7] University of Leiden, PO Box 9513, 2300 RA Leiden, The Netherlands
[8] École Normale Supérieure de Lyon, CRAL, UMR CNRS 5574, Université Lyon I, 46 Allée d'Italie, 69364 Lyon Cedex 07, France
[9] National Radio Astronomy Observatory, 520 Edgemont Rd., Charlottesville, VA 22901, USA
[10] Instituto de Física Fundamental (CSIC), Calle Serrano 123, 28006 Madrid, Spain
[11] Laboratoire d'astrophysique de Bordeaux, Université Bordeaux, CNRS, B18N, allée Geoffroy Saint-Hilaire, 33615 Pessac, France
[12] Leiden Observatory, Leiden University, PO Box 9513, 2300 RA Leiden, The Netherlands
[13] Centro de Astrobiología (CSIC-INTA), Ctra. de Ajalvir, km 4, Torrejón de Ardoz, 28850 Madrid, Spain
[14] Department of Physics, University of Warwick, Coventry, CV4 7AL, UK
[15] Institut des Sciences Moléculaires (ISM), CNRS, Université Bordeaux, 351 cours de la Libération, 33400 Talence, France
[16] Department of Physics, University of Helsinki, PO Box 64, 00014 Helsinki, Finland
[17] Institute of Physics I, University of Cologne, Cologne, Germany
[18] Harvard-Smithsonian Center for Astrophysics, Cambridge, MA 02138, USA
[19] Jeremiah Horrocks Institute, University of Central Lancashire, Preston, PR1 2HE, UK
[20] Chalmers University of Technology, Department of Space, Earth and Environment, 412 93 Gothenburg, Sweden
[21] Departamento de Física, Universidade Federal de Juiz de Fora-UFJF, Juiz de Fora, MG 36036-330, Brazil

Received 15 November 2018 / Accepted 28 February 2019

ABSTRACT

GEMS is an IRAM 30 m Large Program whose aim is determining the elemental depletions and the ionization fraction in a set of prototypical star-forming regions. This paper presents the first results from the prototypical dark cloud Taurus molecular cloud (TMC) 1. Extensive millimeter observations have been carried out with the IRAM 30 m telescope (3 and 2 mm) and the 40 m Yebes telescope (1.3 cm and 7 mm) to determine the fractional abundances of CO, HCO^+, HCN, CS, SO, HCS^+, and N_2H^+ in three cuts which intersect the dense filament at the well-known positions TMC 1-CP, TMC 1-NH3, and TMC 1-C, covering a visual extinction range from $A_V \sim 3$ to ∼20 mag. Two phases with differentiated chemistry can be distinguished: (i) the translucent envelope with molecular hydrogen densities of $1-5\times10^3$ cm^{-3}; and (ii) the dense phase, located at $A_V > 10$ mag, with molecular hydrogen densities $>10^4$ cm^{-3}. Observations and modeling show that the gas phase abundances of C and O progressively decrease along the C^+/C/CO transition zone ($A_V \sim 3$ mag) where C/H $\sim 8\times10^{-5}$ and C/O $\sim 0.8-1$, until the beginning of the dense phase at $A_V \sim 10$ mag. This is consistent with the grain temperatures being below the CO evaporation temperature in this region. In the case of sulfur, a strong depletion should occur before the translucent phase where we estimate an $S/H \sim (0.4–2.2)\times10^{-6}$, an abundance ∼7–40 times lower than the solar value. A second strong depletion must be present during the formation of the thick icy mantles to achieve the values of S/H measured in the dense cold cores ($S/H \sim 8\times10^{-8}$). Based on our chemical modeling, we constrain the value of ζ_{H_2} to $\sim(0.5–1.8)\times10^{-16}$ s^{-1} in the translucent cloud.

Key words. astrochemistry – ISM: abundances – ISM: kinematics and dynamics – ISM: molecules – stars: formation – stars: low-mass

1. Introduction

In recent years, space telescopes such as *Spitzer* and *Herschel* have revolutionized our view of star-forming regions. Images of giant molecular clouds and dark cloud complexes have revealed spectacular networks of filamentary structures where stars are born (André et al. 2010). Interstellar filaments are almost everywhere in the Milky Way and are the preferred site for star formation. Now we believe that filaments precede the onset of most star formation, funneling interstellar gas and dust into increasingly denser concentrations that will contract and fragment, leading to gravitationally bound prestellar cores that will eventually form stars.

Gas chemistry plays a key role in the star formation process by regulating fundamental parameters such as the gas cooling rate, and the gas ionization fraction. Molecular filaments can fragment into prestellar cores to a large extent because molecules cool the gas, thus diminishing the thermal support relative to self-gravity. The ionization fraction controls the coupling of magnetic fields with the gas, driving the dissipation of turbulence and angular momentum transfer, and therefore it plays a crucial role in the cloud collapse (isolated vs. clustered star formation) and the dynamics of accretion disks (see Zhao et al. 2016; Padovani et al. 2013). In the absence of other ionization agents (X-rays, UV photons, J-type shocks), the steady-state ionization fraction is proportional to $\sqrt{\zeta_{H_2}/n}$, where n is the molecular hydrogen density and ζ_{H_2} is the cosmic-ray ionization rate for H_2 molecules, which becomes an essential parameter in molecular cloud evolution (Oppenheimer & Dalgarno 1974; McKee 1989; Caselli et al. 2002). The gas ionization fraction, $X(e^-) = n(e^-)/n_H$, and the molecular abundances depend on the elemental depletion factors (Caselli et al. 1998). In particular, carbon (C) is the main donor of electrons in the cloud surface ($A_V < 4$ mag) and, because of its lower ionization potential and as long as it is not heavily depleted, sulfur (S) is the main donor in the ~3.7–7 magnitude range that encompasses a large fraction of the molecular cloud mass (Goicoechea et al. 2006). Since CO and CII are the main coolants, depletions of C and O determine the gas cooling rate in molecular clouds. Elemental depletions also constitute a valuable piece of information for our understanding of the grain composition and evolution. For a given element X, the missing atoms in gas phase are presumed to be locked up in solids, i.e., dust grains and/or icy mantles. The knowledge of the elemental depletions would hence provide a valuable information to study the changes in the dust grain composition across the cloud. Surface chemistry and the interchange of molecules between the solid and gas phases have a leading role in the gas chemical evolution from the diffuse cloud to the prestellar core phase.

The Gas phase Elemental abundances in Molecular cloudS (GEMS) is an IRAM 30m Large Program whose aim is estimating the S, C, N, O depletions and $X(e^-)$ as a function of visual extinction, in a selected set of prototypical star-forming filaments. Regions with different illumination are included in the sample in order to investigate the influence of UV radiation (photodissociation, ionization, photodesorption) and turbulence (grain sputtering, grain-grain collisions) on these parameters, and eventually in the star formation history of the cloud. This is the first of a series of GEMS papers and it is dedicated to the prototypical dark cloud Taurus molecular cloud (TMC) 1.

2. TMC 1

The TMC, at a distance of 140 pc (Elias 1978; Onishi et al. 2002), is one of the closest molecular cloud complexes, and is considered an archetype of low-mass star-forming regions. It has been the target of several cloud evolution and star formation studies (Ungerechts & Thaddeus 1987; Mizuno et al. 1995; Goldsmith et al. 2008), being extensively mapped in CO (Cernicharo & Guelin 1987; Onishi et al. 1996; Narayanan et al. 2008) and visual extinction (Cambrésy 1999; Padoan et al. 2002). The most massive molecular cloud in Taurus is the Heiles cloud 2 (HCL 2; Onishi et al. 1996). TMC 1 was included in the *Herschel* Gould Belt Survey (André et al. 2010). One first analysis of these data were carried out by Malinen et al. (2012) who generated visual extinction maps of the two long filaments in HCL 2 based on near-IR (NIR) extinction and *Herschel* data. As one of the most extensively studied molecular filament, TMC 1 is also included in the Green-Bank Ammonia Survey (PIs: R. Friesen & J. Pineda; Friesen et al. 2017).

TMC 1 has also been the target of numerous chemical studies. In particular, the positions TMC 1-CP and TMC 1-NH3 (the cyanopolyne and ammonia emission peaks) are generally adopted as templates to compare with chemical codes (Fehér et al. 2016; Gratier et al. 2016; Agúndez & Wakelam 2013). Less studied from the chemical point of view, TMC 1-C has been identified as an accreting starless core (Schnee et al. 2007, 2010).

3. Observational strategy

In order to derive the elemental gas abundance of C, O, N and S, we need to determine the abundances of the main gas reservoirs (see Table 1). Essentially, most of the carbon in molecular clouds is locked in CO and the C depletion is derived from the study of CO and its isotopologues. Several works have studied the depletion of CO in dense starless cores and young protostars (Caselli et al. 1999; Kramer et al. 1999; Bacmann et al. 2002; Alonso-Albi et al. 2010; Hernandez et al. 2011; Maret et al. 2013; Miettinen & Offner 2013; Lippok et al. 2013). The main reservoirs of nitrogen are atomic nitrogen (N) and molecular nitrogen (N_2) which are not observable. The nitrogen abundance needs to be derived by applying a chemical model to fit the observed abundances of nitriles (HCN, HNC, CN) and N_2H^+. The HCN abundance is also dependent on the amount of atomic C in gas phase and hence, on the C/O ratio (Loison et al. 2014). Abundant oxygenated species such as O, O_2, H_2O and OH, cannot be observed in the millimeter domain and the oxygen depletion should be indirectly derived through comparison with chemical models, as well. In the case of sulfur, depending on the local physical conditions and the chemical age, atomic S and/or SO are expected to be the main gas phase reservoir in dense clouds (Fuente et al. 2016; Vidal et al. 2017). Unfortunately, the direct observation of atomic S is difficult and, thus far, has only been detected in some bipolar outflows using the infrared space telescope *Spitzer* (Anderson et al. 2013). Sulfur can also be traced by sulfur recombination lines but they are very weak and not easy to interpret (Roshi et al. 2014). Sulfur depletion in molecular clouds is determined from the observation of a few molecular compounds, mainly CS, HCS^+ or SO (see, e.g., Goicoechea et al. 2006), whose abundances are very sensitive to the C/O gas-phase ratio and also time evolution. Its determination hence requires a good characterization of the gas physical and chemical conditions.

For the present study, we selected a subset of species (CO, HCO^+, HCN, CS, SO, HCS^+ and N_2H^+) that are essential to derive the elemental abundances in the molecular gas. The observations were performed using the receiver setups listed in Table B.1 and the observed molecular transitions are shown in Table B.2. When possible we observe several lines of the

Table 1. Molecular tracers used in this study.

	$A_V < 10$ mag	$A_V > 10$ mag
X(e$^-$)	^{13}CO, HCO$^+$, H^{13}CO$^+$	C^{18}O, HC^{18}O$^+$, N$_2$H$^+$
n(H$_2$)	CS, C^{34}S	C^{34}S, ^{13}CS, SO
C/H	^{13}CO, HCN, CS	C^{18}O, H^{13}CN
O/H	^{13}CO, SO	C^{18}O, SO, ^{34}SO
N/H	HCN	H^{13}CN, N$_2$H$^+$
S/H	CS, C^{34}S, SO, HCS$^+$	C^{34}S, ^{13}CS, SO, ^{34}SO

same species in order to accurately determine the molecular abundance. When only one line was observed, we use the molecular hydrogen density derived from the fitting of the CS (and their rarer isotopologues C^{34}S and ^{13}CS) $3 \rightarrow 2$ and $2 \rightarrow 1$ lines. Towards the edge of the cloud, the densities are lower and the CS $3 \rightarrow 2$ line is not detected. For this reason we complement the 30 m observations with the CS $1 \rightarrow 0$ line as observed with the 40 m Yebes telescope. The 40 m configuration allows us to observe simultaneously the NH_3 (1,1) and (2,2) lines in band K. We use these observations to constrain the gas kinetic temperature at the cloud edges.

The high sensitivity required by our project, prohibits the mapping of a large area. Instead, we observe the three right-ascension cuts covering visual extinctions between $A_V \sim 3$ mag and ~20 mag (see Fig. 1). In details, we have observed 6 positions per cut which corresponds to the offsets (0″,0″), (+30″,0), (+60″,0″), (+120″,0″), (+180″,0″) and (+240″,0″) relative to the positions listed in Table 2, In addition to the 30 m observations, we carried out observations with the 40 m Yebes telescope towards the positions marked with yellow circles in Fig. 1.

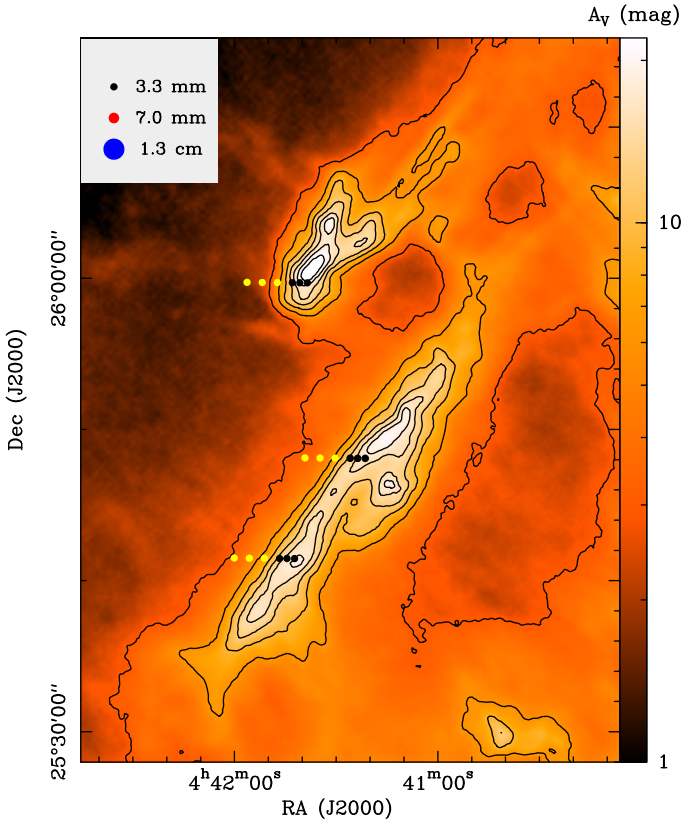

Fig. 1. Visual extinction map of TMC 1 (Kirk et al., in prep.). The positions observed with the 30 m telescope are indicated with circles. Black circles mark positions observed only with the 30 m telescope while yellow circles show the positions observed also with the Yebes 40 m telescope. In the upper left corner, we show the beam of the IRAM telescope at 3 mm (beam ~ 29″) and of Yebes 40 m telescope at 1.3 cm (beam ~ 84″) and at 7 mm (beam ~ 42″). Contours are 3, 6, 9, 12, 15, and 18 mag.

4. Data acquisition

4.1. IRAM 30 m telescope

The 3 and 2 mm observations were carried out using the IRAM 30-m telescope at Pico Veleta (Spain) during three observing periods in July 2017, August 2017 and February 2018. The telescope parameters at 3 and 2 mm are listed in Table B.1 with the beam size varying with the frequency as $HPBW('') = 2460/\nu$ where ν is in GHz. The observing mode was frequency switching with a frequency throw of 6 MHz well adapted to remove standing waves between the secondary and the receivers. The Eight MIxer Receivers (EMIR) and the Fast Fourier Transform Spectrometers (FTS) with a spectral resolution of 49 kHz were used for these observations. The intensity scale is T_{MB} which is a good estimate of T_B as long as the source size is comparable to the observational beam. In our case, the emission is expected to be more extended. In the limiting case of the source being extended through the whole sky, the correct intensity scale would be T_A^*, where T_{MB} and T_A^* are related by $T_{MB} = (F_{eff}/B_{eff})T_A^*$ (see Table B.1). Since the difference between one scale and the other is not large, ≈17% at 86 GHz and 27% at 145 GHz, we adopt the T_{MB} scale. The uncertainty in the source size is included in the line intensity errors which are assumed to be ~20%. Although numerous lines are detected in the range of frequencies covered by our observations, in this paper we concentrate on the most abundant molecules (and their isotopologues): CO, HCO$^+$, HCN, CS, SO, HCS$^+$ and N$_2$H$^+$. Other species will be analyzed in forthcoming papers.

Table 2. Source coordinates.

	RA (J2000)	Dec (J2000)	V_{lsr} (km s^{-1})
TMC 1-CP	04^{h}41^{m}41^s.90	25°41′27.″1	5.8
TMC 1-NH3	04^{h}41^{m}21^s.30	25°48′07.″0	5.8
TMC 1-C	04^{h}41^{m}38^s.80	25°59′42.″0	5.2

4.2. Yebes 40 m telescope

The RT40m is equipped with HEMT receivers for the 2.2–50 GHz range, and an SIS receiver for the 85–116 GHz range. Single-dish observations in K-band (21–25 GHz) and Q-band (41–50 GHz) can be performed simultaneously. This configuration was used to observe the positions marked with a yellow circle in Fig. 1. The backends consisted of FFTS covering a bandwidth of ~2 GHz in band K and ~9 GHz in band Q, with a spectral resolution of ~38 kHz. Central frequencies were 23 000 and 44 750 MHz for the K and Q band receivers, respectively. The observing procedure was position-switching, and the OFF-positions are RA(J2000) = 04^{h}42^{m}24^s.24 Dec(2000) = 25°41′27.″6 for TMC 1-CP, RA(J2000) = 04^{h}42^{m}29^s.52 Dec(2000) = 25°48′07.″2 for TMC 1-NH3, RA(J2000) = 04^{h}42^{m}32^s.16 Dec(J2000) = 25°59′42.″0 for TMC 1-C. These positions were checked to be empty of emission before the

observations. The intensity scale is $T_{\rm MB}$ with conversion factors of 4.1 Jy K^{-1} in band K ($T_{\rm MB}/T_A^* = 1.3$) and in 5.7 Jy K^{-1} in band Q ($T_{\rm MB}/T_A^* = 2.1$). The HPBW of the telescope is 42″ at 7 mm and 84″ at 1.3 cm (Table B.1).

4.3. Herschel space observatory: A_V and T_d maps

In this work, we use the column density and dust temperature maps of TMC 1 created following the process described in Kirk et al. (2013, and in prep.). In the following, we give a brief explanation of the methodology. The PACS and SPIRE (Poglitsch et al. 2010; Griffin et al. 2010) data were taken as part of the *Herschel* Gould Belt Survey (André et al. 2010) and were reduced as described in Kirk et al. (in prep.). The absolute calibration (median flux level) of the maps was estimated using data from *Planck* and IRAS (cf. Bernard et al. 2010). The data was then convolved to the resolution of the longest wavelength 500 μm (36 arcsec).

A modified blackbody function of the form $F_\nu = MB_\nu(T)\kappa_\nu/D^2$ was fitted to each point where M is the dust mass, $B_\nu(T)$ is the Planck function at temperature T and $D = 140$ pc was the assumed distance to Taurus. The dust mass opacity was assumed to follow a standard law, $\kappa_\nu \propto \nu^\beta$, with $\beta = 2$ and a reference value of 0.1 cm^2 g^{-1} at $\lambda = 1$ THz (Beckwith et al. 1990). When using the same dust assumptions, the resulting dust map agreed well with the *Planck* 353 GHz Optical Depth map above $N(\rm H_2) \sim 1.5 \times 10^{21}$ cm^{-2} (Kirk et al., in prep.). The typical uncertainty on the fitted dust temperature was 0.3–0.4 K. The uncertainty on the column density was typically 10% and reflects the assumed calibration error of the *Herschel* maps (Kirk et al., in prep.).

5. Spectroscopic data: line profiles

Figures B.1–B.3 show a subset of our spectra across the cuts TMC 1-CP, TMC 1-NH3 and TMC 1-C. The lines of the most abundant species are optically thick at $A_{\rm V} > 7$ mag and present self-absorbed profiles. However, only the lines of the main isotopologue are detected towards positions with $A_{\rm V} < 7$ mag. Linewidths vary between ~0.3 and ~1.5 km s^{-1} depending on the transition. The largest line widths are measured in the ^{13}CO $1 \rightarrow 0$ lines with $\Delta v \sim 1.5 \pm 0.5$ km s^{-1}. The higher excitation lines of species like CS and SO, and those of the high dipole moment tracers HCS$^+$, N_2H^+ and HCN, show $\Delta v \sim 0.4 \pm 0.1$ km s^{-1}. Similar linewidths are observed in the NH_3 (1,1) and (2,2) inversion lines. Line broadening because of high optical depths might explain, at least partially, the large linewidths observed in the ^{13}CO and CS lines. High optical depths are also measured in the HCN $1 \rightarrow 0$ lines but the linewidth remains narrow, $\Delta v \sim 0.4 \pm 0.1$ km s^{-1}. The narrow HCN linewidths are better understood as the consequence of the existence of layers with different excitation and hence chemical conditions along the line of sight.

Several authors have discussed the complex velocity structure of the TMC 1 cloud (Lique et al. 2006a; Fehér et al. 2016; Dobashi et al. 2018). Based on high-velocity resolution ($\delta v_{\rm lsr} = 0.0004$ km s^{-1}) observations of the HC_3N $J = 5 \rightarrow 4$ line, Dobashi et al. (2018) propose that the dense TMC 1 filament is composed of at least 4 velocity components at $v_{\rm lsr} = 5.727$, 5.901, 6.064 and 6.160 km s^{-1} with small linewidths, ~0.1 km s^{-1}, and a more diffuse component at 6.215 km s^{-1} with a linewidth of ~0.5 km s^{-1}. The velocity resolution of our observations (from 0.27 km s^{-1} at 7 mm, to 0.16 km s^{-1} at 3 mm and 0.09 km s^{-1} at 2 mm) is not enough to resolve these narrow velocity components. In spite of this, in order to have a deeper insight in the velocity structure of the region, we have fitted the observed profiles using 5 velocity components centered at $v_{\rm lsr} = 5.0$, 5.5, 6.0, 6.5, 7.0 km s^{-1} and with a fixed $\Delta v = 0.5$ km s^{-1}. Figure 2 shows the result of our fitting for three positions, offsets (+240″,0), (+120″,0) and (0,0) in the cut across TMC 1-CP. Interestingly, the number of velocity components detected in each transition remains constant with the position, even when the position (+240″,0) is located 0.16 pc away from TMC 1-CP. However, the number of detected velocity components does vary from one transition (and species) to another. The five velocity components appear in the spectra of ^{13}CO $1 \rightarrow 0$, C^{18}O $1 \rightarrow 0$ and HCO$^+$ $1 \rightarrow 0$. The CS $2 \rightarrow 1$ and SO $2_3 \rightarrow 1_2$ spectra present intense emission in the 5.5 and 6.0 km s^{-1} components and weak wings at the velocity of the other components. Interestingly, only the 5.5 km s^{-1} component presents intense emission in the HCN spectra. As a first approximation, in this paper we use the integrated line intensities to derive column densities and abundances. This is motivated by the limited spectral resolution (at 3 mm) and sensitivity (at 2 mm) of our observations that would introduce large uncertainties in the multi-velocity analysis.

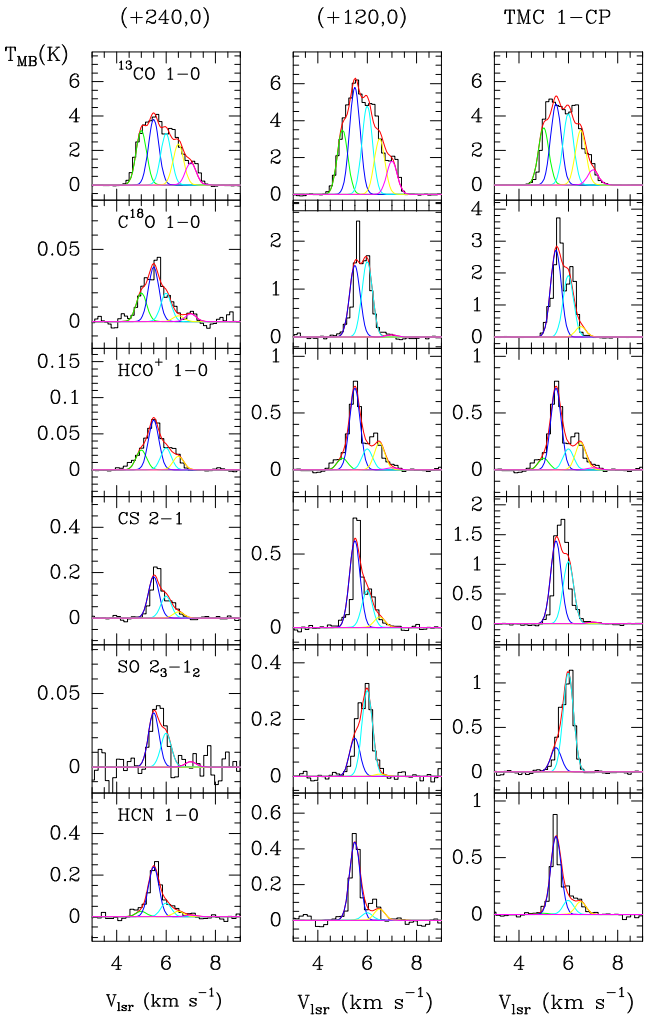

Fig. 2. Selection of 30 m spectra towards the offsets (+240″,0), (120″,0) and (0,0) in the TMC 1-CP cut. In order to investigate the velocity structure we have fitted the observed line profiles with 5 Gaussians with a fixed linewidth of 0.5 km s^{-1}, each centered at the velocities 5.0 (green), 5.5 (dark blue), 6.0 (light blue), 6.5 (yellow) and 7.0 km s^{-1} (fuchsia).

Table 3. Physical conditions.

Position	HSO (Kirk+19)		GEMS (This work)		NH_3 (Fehér + 16)		Species and transitions used in the calculations
	T_d (K)	N(H_2) ($\times 10^{21}$ cm^{-2})	T_k (K)	$n(H_2)$ ($\times 10^4$ cm^{-3})	T_k (K)	$n(H_2)$ ($\times 10^4$ cm^{-3})	
TMC1-CP+0	11.92	18.20	9.7 ± 0.8	1.5 ± 0.4	10.6 ± 1.1	1.0 ± 0.3	^{13}CS–C^{34}S $J = 2 \rightarrow 1, 3 \rightarrow 2$
TMC1-CP+30	12.00	16.71	10.2 ± 0.2	2.3 ± 0.3			^{13}CS–C^{34}S $J = 2 \rightarrow 1, 3 \rightarrow 2$
TMC1-CP+60	12.24	13.74	11.2 ± 2.0	3.7 ± 1.9			^{13}CS–C^{34}S $J = 2 \rightarrow 1, 3 \rightarrow 2$
TMC1-CP+120	13.16	7.27	12.5 ± 1.2	0.15 ± 0.04			C^{34}S–CS $J = 1 \rightarrow 0, 2 \rightarrow 1, 3 \rightarrow 2$
TMC1-CP+180	13.86	4.77	16.0 ± 3.0	0.27 ± 0.09			C^{34}S–CS $J = 1 \rightarrow 0, 2 \rightarrow 1, 3 \rightarrow 2$
TMC1-CP+240	14.39	3.25	14.7 ± 1.1	0.16 ± 0.10			CS $J = 1 \rightarrow 0, 2 \rightarrow 1, 3 \rightarrow 2$
TMC1-NH3+0	11.70	16.97	11.8 ± 2.8	2.0 ± 1.0	11.0 ± 1.1	1.2 ± 0.3	^{13}CS–C^{34}S $J = 2 \rightarrow 1, 3 \rightarrow 2$
TMC1-NH3+30	11.79	15.58	10.2 ± 2.8	1.2 ± 0.8			^{13}CS–C^{34}S $J = 2 \rightarrow 1, 3 \rightarrow 2$
TMC1-NH3+60	12.12	12.88	12.7 ± 1.1	1.5 ± 0.8			^{13}CS–C^{34}S $J = 2 \rightarrow 1, 3 \rightarrow 2$
TMC1-NH3+120	13.10	10.04	11.9 ± 1.6	0.29 ± 0.14			C^{34}S–CS $J = 1 \rightarrow 0, 2 \rightarrow 1, 3 \rightarrow 2$
TMC1-NH3+180	13.78	4.04	11.4 ± 1.4	0.16 ± 0.06			CS $J = 1 \rightarrow 0, 2 \rightarrow 1, 3 \rightarrow 2$
TMC1-NH3+240	13.10	2.18	13.5 ± 2.3	0.29 ± 0.19			CS $J = 1 \rightarrow 0, 2 \rightarrow 1, 3 \rightarrow 2$
TMC1-C+0	11.26	19.85	8.5 ± 2.0	4.5 ± 3.4			^{13}CS–C^{34}S $J = 2 \rightarrow 1, 3 \rightarrow 2$
TMC1-C+30	11.32	18.47	10.3 ± 2.0	4.3 ± 2.3			^{13}CS–C^{34}S $J = 2 \rightarrow 1, 3 \rightarrow 2$
TMC1-C+60	11.67	13.34	11.6 ± 2.2	1.19 ± 0.45			^{13}CS–C^{34}S $J = 1 \rightarrow 0, 2 \rightarrow 1, 3 \rightarrow 2$
TMC1-C+120	13.13	4.79	11.1 ± 1.9	0.29 ± 0.10			C^{34}S–CS $J = 1 \rightarrow 0, 2 \rightarrow 1, 3 \rightarrow 2$
TMC1-C+180	14.08	2.20	13.5 ± 1.1	0.55 ± 0.28			C^{34}S–CS $J = 1 \rightarrow 0, 2 \rightarrow 1, 3 \rightarrow 2$
TMC1-C+240	14.53	1.63	13.5 ± 2.7	0.26 ± 0.18			CS $J = 1 \rightarrow 0, 2 \rightarrow 1, 3 \rightarrow 2$

Taking into account the analysis of the line profiles described in this section, we can conclude that our results probe the moderate to high-density gas detected at $V_{lsr} = 5.5$ and 6.0 km s^{-1}.

6. Physical conditions: gas kinetic temperature and molecular hydrogen density

A detailed knowledge of the physical conditions is required for an accurate estimate of the molecular column densities and abundances. This is specially important in those positions where we have observed only one line and a multi-transition study is not possible. In these cases, the knowledge of the gas kinetic temperature and density is imperative. CS is a diatomic molecule with well known collisional coefficients (Denis-Alpizar et al. 2018; Lique et al. 2006b) that has been largely used as density and column density tracer in the interstellar medium. Moreover, the velocity-component analysis presented in Sect. 5 shows that CS is detected in the 5.5 and 6.0 km s^{-1} components, which encompass the bulk of the dense molecular gas (compare, e.g., the C^{18}O and CS profiles in Fig. 2). Therefore, we consider that CS and its isotopologues are good tracers of the average physical conditions in this cloud.

In order to derive the gas physical conditions, we fit the line intensities of the observed CS, C^{34}S and ^{13}CS lines using the molecular excitation and radiative transfer code RADEX (van der Tak et al. 2007). During the fitting process, we fix the isotopic ratios to ^{12}C/^{13}C = 60, ^{32}S/^{34}S = 22.5 (Gratier et al. 2016) and assume a beam filling factor of 1 for all transitions (the emission is more extended than the beam size). Then, we let T_k, $n(H_2)$ and N(CS) vary as free parameters. The parameter space (T_k, $n(H_2)$ and N(CS)) is then explored following the Monte Carlo Markov Chain (MCMC) methodology with a Bayesian inference approach. In particular, we used the emcee (Foreman-Mackey et al. 2013) implementation of the Invariant MCMC Ensemble sampler methods by Goodman & Weare (2010). While $n(H_2)$ and N(CS) are allowed to vary freely, we need to use a prior to limit the gas kinetic temperatures to reasonable values in this cold region and hence break the temperature-density degeneracy that is usual in this kind of calculations.

The prior in the gas kinetic temperature is based on our knowledge of the dust temperature from *Herschel* maps (Kirk et al., in prep.). Gas and dust are expected to be thermalized in regions with $n(H_2) > 10^4$ cm^{-3}. Friesen et al. (2017) estimated the gas kinetic temperature in a wide sample of molecular clouds based on the NH_3 (1,1) and (2,2) inversion lines, and obtained that the gas temperature is systematically ~1–2 K lower than the dust temperature obtained from the *Herschel* maps. This discrepancy is interpreted as the consequence of the single-temperature SED fitting procedure which assumes that all the dust is at the same temperature along the line of sight. Towards a starless core in which the dust in the surface is warmer than in the innermost region, this approximation would produce an overestimation of the dust temperature. In order to account for these effects, in our MCMC calculations we use a flat prior to the gas kinetic temperature with constant probability for $T_k = T_d \pm 5$ K and zero probability outside.

In Table 3, we show the gas temperature and the density derived from the multi-line fitting of CS and its isotopologues. Across the cuts, there are two differentiated regions: (i) for $A_V < 7.5$ mag, the density is quite uniform and similar to a few 10^3 cm^{-3} and gas temperatures are about 13–15 K which corresponds to gas thermal pressure of $\sim 5 \times 10^4$ K cm^{-3}. Hereafter, we will refer to this moderate density envelope as the translucent component; and (ii) for $A_V > 7.5$ mag, the density is an order of magnitude larger, $T_k \sim 10$ K and the density keeps increasing towards the extinction peak. Hereafter, we will refer to this region as the dense component. The gas pressure in the dense phase is about 10 times larger than in the translucent phase. The transition from one phase to the other occurs in <60″ (~0.04 pc) and it is not well sampled by our data (see Fig. 3).

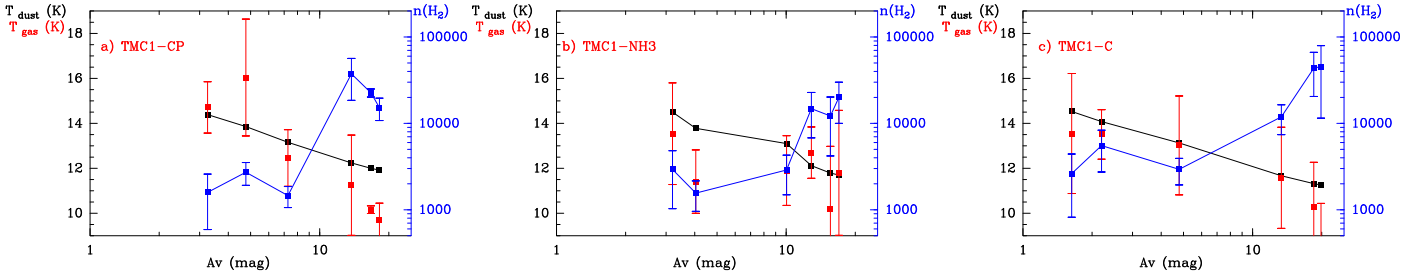

Fig. 3. Estimated values of the dust temperature (black) as derived from Kirk et al. (in prep.), gas temperature (red) and molecular hydrogen density (blue) across the cuts through TMC 1-CP (*panel a*), TMC 1-NH3 (*panel b*) and TMC 1-C (*panel c*).

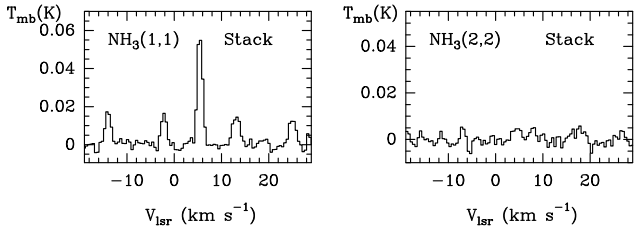

Fig. 4. NH_3 (1,1) and NH_3 (2,2) lines profiles obtained by stacking all the band-*K* spectra observed with the 40 m Yebes telescope (A_V < 10 mag) towards TMC 1.

Table 4. Collisional rate coefficients.

Mol.		Ref.
CO	p-H_2	Yang et al. (2010)
HCO^+	p-H_2	Flower (1999)
HCN	p-H_2	Ben Abdallah et al. (2012)
CS	p-H_2	Denis-Alpizar et al. (2018)
	He	Lique et al. (2006b)
SO	p-H_2	Lique & Spielfiedel (2007)
N_2H^+	p-H_2	Daniel et al. (2016)

The low densities found in the translucent phase, $n(H_2)$ approximately a few 10^3 cm^{-3}, might cast some doubts about our assumption of gas and dust thermal equilibrium. In order to check this hypothesis, we have tried to independently derive the gas kinetic temperature in this region using our NH_3 data. For that, we have stacked all the NH_3 (1,1) and (2,2) spectra obtained with the 40 m Yebes telescope towards the positions with A_V < 10 mag of the three cuts. The stacked spectra are shown in Fig. 4, with a good detection of the NH_3 (1,1) line while the NH_3 (2,2) line remains undetected. Even assuming a density as low as $n(H_2) = 10^3$ cm^{-3}, a RADEX calculation shows that the non-detection of the (2,2) line implies an upper limit of <15 K for the gas temperature, slightly lower than the dust temperature. It is remarkable that NH_3 is only detected in the 5.5 km s^{-1} velocity component while CS is detected in the 5.5 and 6.0 km s^{-1} components. The upper limit to the gas kinetic temperature is only valid for the 5.5 km s^{-1} component that is very likely the densest and coldest component. We consider, therefore, that the temperature derived from the CS fitting is more adequate for our purposes and it is used hereafter in the molecular abundance calculations. In Sect. 8, we show that the temperatures obtained with our CS fitting are in good agreement with those predicted with the Meudon PDR code.

Another important assumption in our density estimate process is that the beam filling factor is 1 for all the transitions. This is based on the morphology of the *Herschel* maps that present smooth and extended emission in the translucent part. This assumption is questionable towards the extinction peaks where the column density map presents a steeper gradient (see Fig. 1). In Table 3 we also compare our estimates with previous ones by Fehér et al. (2016) towards TMC 1-CP and TMC 1-NH3, finding excellent agreement. The good agreement between our estimates and those derived from NH_3, which are not affected by different beam sizes, suggests that our assumption is not far from the reality. The derived densities for the translucent component are in good agreement with previous estimates of the envelope density by Schnee et al. (2010) and Lique et al. (2006a).

7. Molecular abundances

Beam averaged molecular column densities and abundances have been derived using RADEX and the collisional rate coefficients shown in Table 4. In the following, we add more details of the abundance calculations.

7.1. ^{13}CO, $C^{18}O$

In this work, we use ^{13}CO and C^{18}O as tracers of CO by assuming fixed isotopic ratios. We use the physical conditions in Table 3 to derive ^{13}CO and C^{18}O column densities from the observations of the $J = 1 \rightarrow 0$ rotational line. This line is thermalized in the range of densities considered, therefore we do not expect any uncertainty in the molecular abundances because of the adopted densities. The major uncertainty comes from the opacity effects and possible variations in the CO/C^{18}O and CO/^{13}CO ratios.

For $A_V > 7$ mag, the ^{13}CO $1 \rightarrow 0$ line is expected to be optically thick ($\tau > 1$). In this region, we use C^{18}O as tracer of the CO abundance by assuming ^{16}O/^{18}O = 600 (Wilson & Rood 1994). For $A_V < 7$ mag, the ^{13}CO line is expected to be optically thin. In this region, we have separately estimated the ^{13}CO and C^{18}O column densities which allows us to investigate the $N(^{13}CO)/N(C^{18}O)$ ratio. Interestingly, this ratio increases from ~10 at $A_V \sim 7$ mag to ~40 at $A_V \sim 3$ mag. This result is not the consequence of the numerous velocity components along the line of sight. As shown in Fig. 2, the $T_b(^{13}CO\ 1 \rightarrow 0)/T_b(C^{18}O\ 1 \rightarrow 0)$ is >20 in all the velocity components towards the offset (240″,0). Similarly $T_b(^{13}CO\ 1 \rightarrow 0)/T_b(C^{18}O\ 1 \rightarrow 0) \sim 4$ in all velocity components towards the offset (120″,0). The high $N(^{13}CO)/N(C^{18}O)$ ratio is more likely the consequence of selective photodissociation and isotopic fractionation in the translucent cloud (Liszt & Lucas 1996; Bron et al. 2018). Because of isotopic fractionation in the external part of the cloud, a reliable estimate of $N(^{12}CO)$ requires the comparison with a chemical model that includes a differentiated chemistry for the CO

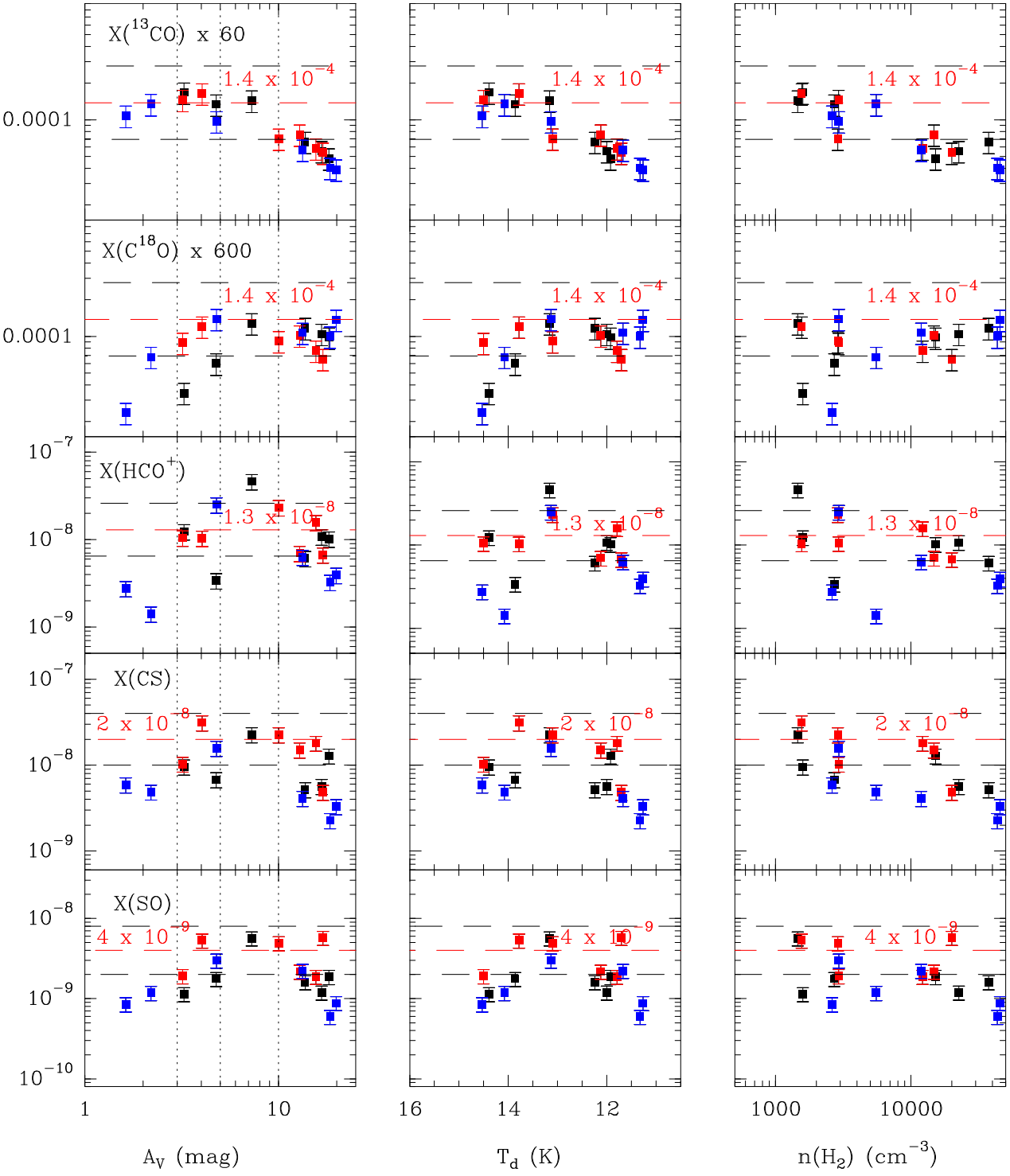

Fig. 5. Estimated molecular abundances with respect to H_2 for the three studied cuts, TMC 1-CP (black squares), TMC 1-NH3 (red) and TMC 1-C (blue) as a function of the visual extinction (*left panel*), dust temperature (*center panel*) and molecular hydrogen densities (*right panel*). The horizontal lines indicate a representative value in the translucent part (red dashed line) and a variation of a factor of 2 relative to it (black dashed lines). Vertical lines mark $A_V = 3$, 5, and 10 mag.

isotopologues. We will discuss this phenomenon in Sect. 8 when we compare our results with the Meudon PDR code predictions.

In Fig. 5, we plot the CO abundance derived as $X(^{13}CO) \times 60$ and $X(C^{18}O) \times 600$ as a function of visual extinction, dust temperature and density in the three observed cuts. The decrease of the ^{13}CO abundance for $A_V > 10$ mag is not real but the consequence of the high optical depth of the observed lines. In this dense regions, the rarer isotopologue $C^{18}O$ is a better tracer of the CO abundance. The $C^{18}O$ abundance sharply decreases for $A_V < 3$ mag. This is consistent with the threshold of $A_V = 1.5$ mag proposed by Cernicharo & Guelin (1987) for the $C^{18}O$ detection. The CO abundance presents a peak of $\sim 1.4 \times 10^{-4}$ at $A_V \sim 3$ mag ($T_d = 14$ K) and seems to decrease towards the dense core phase. This is the expected behavior in

this dark cloud where the dust temperature is lower than the evaporation temperature (T_{evap} = 15–25 K), so that freeze-out is expected.

7.2. HCO^+, $H^{13}CO^+$, $HC^{18}O^+$

We have observed the $J = 1 \rightarrow 0$ rotational lines of HCO^+, $H^{13}CO^+$ and $HC^{18}O^+$. Column densities of all isotopologues have been derived using RADEX and the physical parameters in Table 3. In our column density calculations, we only use the $H^{13}CO^+$ and $HC^{18}O^+$ spectra because the HCO^+ $J = 1 \rightarrow 0$ line presents self-absorbed profiles. Then, we derive the HCO^+ column density from the rarer isotopologues assuming $N(HCO^+)/N(H^{13}CO^+) = 60$ or $N(HCO^+)/N(HC^{18}O^+) = 600$. The results are shown in Fig. 5. The HCO^+ abundance is maximum at $A_V \sim 5$–10 mag, i.e., 2 mag deeper than CO in the translucent cloud. The abundance of HCO^+ further decreases towards the dense high extinctions peaks.

7.3. CS, $C^{34}S$, ^{13}CS

The CS column densities have been derived as explained in Sect. 6. We find that the CS abundance is maximum at $A_V \sim 5$–10 mag, with abundances with respect to H_2, X(CS) $\sim 2 \times 10^{-8}$. The dispersion in the derived CS abundances in translucent cloud is of a factor of 2. For $A_V > 10$ mag, the CS abundance sharply decreases suggesting a rapid chemical destruction or freeze out on the grain mantles.

7.4. SO, ^{34}SO

Several lines of SO and ^{34}SO lie in the frequency range covered by our setups (see Table B.2). Regarding ^{34}SO, only the $J = 2_3 \rightarrow 1_2$ has been detected towards the high extinction positions of the TMC 1-CP, TMC 1-NH3 and TMC 1-CP cuts. Towards the positions where we detect this ^{34}SO line, we measure $T_b(SO\ 2_3 \rightarrow 1_2)/T_b(^{34}SO\ 2_3 \rightarrow 1_2)$ of 10–20. This implies opacities < 2, i.e., the emission is moderately optically thick in the dense region. We have estimated the SO column density based on the RADEX fitting of the main isotopologue lines in the dense and translucent phases. Towards the high extinction peaks, we estimate an uncertainty of a factor of 2 in the column density estimates because of the moderate opacity. The derived SO abundances are $\sim 1.8 \times 10^{-9}$, 0.9×10^{-9} and 2.9×10^{-9} for TMC 1-CP, TMC 1-C and TMC 1-NH3, respectively. Towards the dense phase, we have been able to derive the density from the $T_b(SO\ 3_4 \rightarrow 2_3)/T_b(SO\ 2_3 \rightarrow 1_2)$ ratio, obtaining values fully consistent with those in Table 3. Our abundance estimate towards TMC 1-CP is consistent with previous estimates by Ohishi & Kaifu (1998), Agúndez & Wakelam (2013) and Gratier et al. (2016). The overabundance of SO towards TMC 1-NH3 has been already pointed out by several authors (Lique et al. 2006a and references therein). Similarly to HCO^+ and CS, SO presents its maximum abundance at $A_V \sim 5$–10 with a peak value of $\sim 5 \times 10^{-9}$.

7.5. HCS^+

Because of the weak intensities of the HCS^+ lines, we have only detected one line per position which prevents a multi-transition study. In order to estimate the HCS^+ abundances we have assumed the physical conditions in Table 3 and used the HCO^+ collisional rate coefficients. We obtain a large scatter in the HCS^+ abundances in the whole range of visual extinctions (see Fig. 6), without any clear trend of the HCS^+ abundance with the visual extinction, dust temperature or gas density. Interestingly, we find differences among the HCS^+ abundance towards the different cuts, being larger towards TMC 1-CP than towards TMC 1-NH3 and TMC 1-C (see Fig. 6).

7.6. HCN, $H^{13}CN$, $HC^{15}N$, N_2H^+

All the N-bearing species included in this subsection share some characteristics: (i) they are only detected in the 5.5 km s^{-1} component and (ii) present larger abundances towards the dense phase than towards the outer part of the cloud.

The hyperfine splitting of HCN allows us to estimate the opacity and excitation temperature (assuming a beam filling factor of 1 and equal excitation temperature for all the hyperfine components) and hence, to obtain an estimate of the density and column density. In the dense region, the HCN $1 \rightarrow 0$ line presents deep self-absorption features (see Figs. B.1, B.2 and B.3). Thus, we use the isotopologue $H^{13}CN$ to calculate the gas density and X(HCN) assuming N(HCN)/N($HC^{13}CN$) = 60. We obtain HCN abundances of $2-10 \times 10^{-9}$ and molecular hydrogen densities of a few $\times 10^5$ cm^{-3} in the dense cloud. It is remarkable that the densities derived from the HCN data are larger than those derived from CS and NH_3 by a factor of >10.

Relatively intense emission of the HCN $1 \rightarrow 0$ line is detected in the translucent cloud. Because of the large dipole moment of HCN, molecular hydrogen densities $>10^4$ cm^{-3} are required to achieve excitation temperatures >5 K and hence detectable emission. One possibility is that the densities in the 5.5 km s^{-1} component of the translucent cloud are $n(H_2) > 10^4$ cm^{-3}. In fact, following the procedure described above, we derive densities approximately a few 10^4 cm^{-3} and X(HCN)$\sim 1 \times 10^{-9}$ (see Fig. 6) in the $3 < A_V < 10$ mag range. Alternatively, radiative trapping could have an important role in the excitation of the HCN $1 \rightarrow 0$ line in TMC 1. Radiative excitation would explain the excitation of the HCN line without invoking higher densities in the 5.5 km s^{-1} velocity component. Assuming a core/envelope system (two-phase model) and using a Monte Carlo radiative transfer code, Gonzalez-Alfonso & Cernicharo (1993) explained the line intensities in TMC 1 with HCN abundances of $\sim 5 \times 10^{-9}$ all across the cloud. In this two-phase model, the HCN molecules in the envelope are excited by the photons coming from the core which is a bright source in the HCN $1 \rightarrow 0$ line without the need of invoking higher densities. The value thus derived by Gonzalez-Alfonso & Cernicharo (1993) is similar to that we have derived for the dense gas and a factor of ~5 larger than the HCN abundances we derive in the translucent cloud. Comparing with these results, we consider that our estimates of the HCN abundance based on one-phase molecular excitation calculations are accurate within a factor of 5–10.

Similarly to HCN, we have fitted the excitation temperature and opacity of the N_2H^+ $1 \rightarrow 0$ line based on the hyperfine splitting, and hence the total N_2H^+ column densities. This molecular ion has been almost exclusively detected towards the dense region with abundances of about 1×10^{-9} and densities of a few 10^4 cm^{-3}, quite consistent with those derived from CS. Towards the translucent cloud, we have detections only for $A_V > 5$ mag with abundances of $\sim 5 \times 10^{-10}$.

8. Chemical modeling of the translucent cloud

The increase in dust temperature at the edges of molecular clouds is understood as the consequence of dust heating by the surrounding interstellar radiation field (IRSF). Moreover, the high $N(^{13}CO)/N(C^{18}O)$ ratio measured in TMC 1 testifies that UV radiation has an active role in the molecular chemistry. To

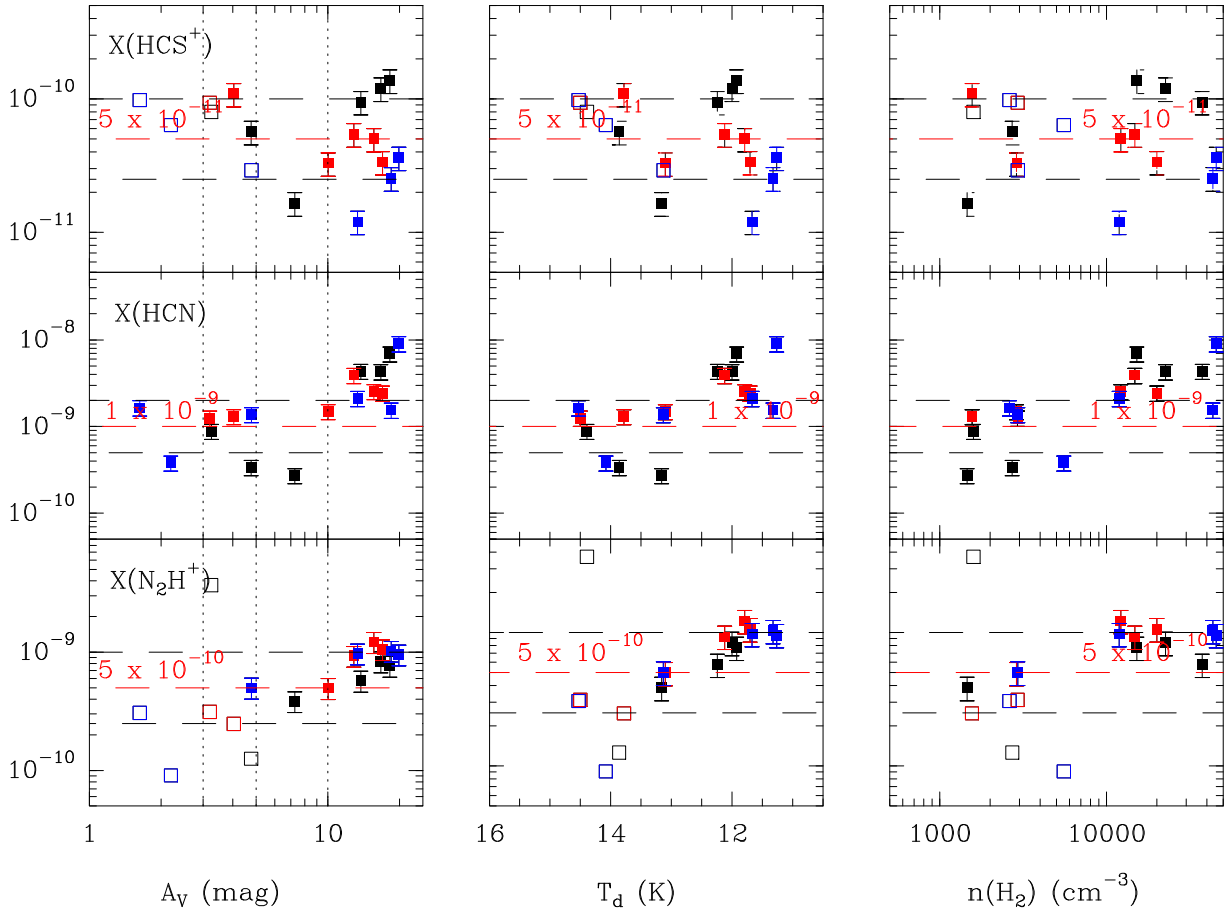

Fig. 6. Estimated molecular abundances with respect to H_2 for the three studied cuts, TMC 1-CP (black squares), TMC 1-NH3 (red) and TMC 1-C (blue) as a function of the visual extinction (*left panel*), dust temperature (*center panel*) and molecular hydrogen densities (*right panel*). Empty symbols correspond to upper limits. The horizontal lines indicate a representative value in the translucent part (red dashed line) and a variation of a factor of 2 relative to it (black dashed lines). Vertical lines mark $A_V = 3$, 5, and 10 mag.

determine the value of the ambient UV field is hence a requisite for the appropriate chemical modeling of the region.

8.1. Estimate of the incident UV field in TMC 1: dust temperature

Herschel has provided extensive H_2 column density and dust temperature maps, with high angular resolution (~36″), of nearby star-forming regions. These maps constitute an unprecedented opportunity to determine the incident UV field and its local variations due to the nearby star formation activity. Dust temperatures are established by the radiative equilibrium balance between the absorption of UV/visible photons and the emission at a given temperature, T_d. In the cloud border, the exact value of T_d depends on the local IRSF and the absorption efficiencies of grains that are dependent on the grain composition and size. Deeper in the cloud, grain heating is produced by near and mid-infrared emission coming from the warm dust layer at the surface of the cloud (Zucconi et al. 2001). The direct calculation of the local UV field as a function of the dust temperature is hampered by our poor knowledge of the grain composition and its detailed variation across the cloud. Another fundamental problem is that in our part of the Galaxy the dust heating is dominated by the visible part of the ISRF, and the visible/IR part of the ISRF does not scale in a simple way with the ultraviolet part. Hence, the UV field derived from the dust temperature can only be considered as a a first guess of the local UV flux.

Different attempts have been done to derive parametric expressions that relates the UV ambient field and the dust temperature as a function of the visual extinction (Hollenbach et al. 1991; Zucconi et al. 2001; Garrod & Pauly 2011; Hocuk et al. 2017). Most of them provide a good fitting of the observed T_d as a function of the incident UV field, χ_{UV}, in a given range of visual extinctions but have problems to fit the whole range, from $A_V = 0.01$ to $A_V > 50$ mag. We have used the most recent parametric expression by Hocuk et al. (2017) to obtain an estimate of the incident UV field. This expression is well adapted to the range of visual extinctions relevant to this paper (3 mag $< A_V <$ 20 mag) and is consistent with what one would expect for a mixed carbonaceous-silicate bared grains.

$$T_d = [11 + 5.7 \times \tanh(0.61 - \log10(A_V))]\, \chi_{UV}^{1/5.9}, \quad (1)$$

where χ_{UV} is the UV field in Draine units and the visible/IR part of the IRSF is assumed to scale with χ_{UV}.

Figure 7 shows the T_d–A_V plots for the 3 cuts considered in this paper. None of the cuts can be fitted with a single value of the UV field. In fact, the dense cloud ($A_V > 7.5$ mag) is better fitted with $\chi_{UV} \sim 10$ while the translucent cloud is fitted with $\chi_{UV} \sim 3$. Moreover, the three observed cuts share the same behavior (see Fig. 7). One compelling possibility is that this break at $A_V \sim 7.5$ mag is caused by a change in the grain properties. A thick layer of ice would allow the dust to be warmer by up to 15% at visual extinctions >10 mag, i.e., the dense component

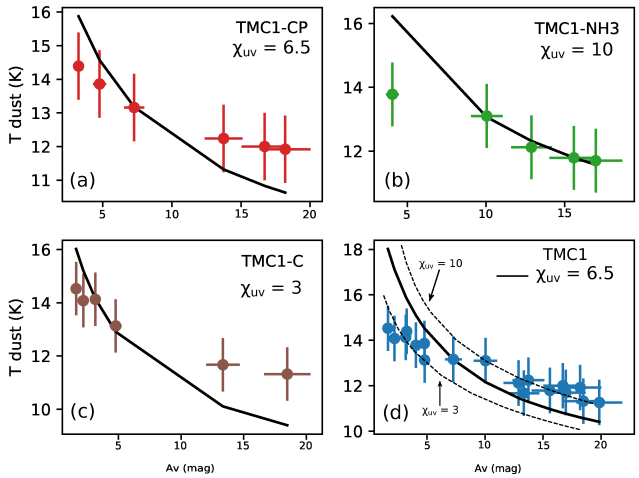

Fig. 7. T_d–A_V fit following the parametric expression published by Hocuk et al. (2017) for the observed cuts: TMC 1-CP in *panel a*, TMC 1-NH3 in *panel b* and TMC 1-C in *panel c*. In *panel d*, we try to fit all the positions from the three cuts together. For $A_V < 7.5$ mag, the best fit is found for $\chi_{UV} \sim 3$. For $A_V > 7.5$ mag, the best fit corresponds to $\chi_{UV} \sim 10$. The average value of $\chi_{UV} \sim 6.5$ is found to provide the best fit for the whole TMC 1 region.

(Hocuk et al. 2017). In fact, if we decrease the dust temperature in the dense regions by this factor, we could explain all the positions with $\chi_{UV} \sim 3$. This interpretation is also consistent with the sharply decrease in the abundances of the C- and S-bearing molecules with visual extinction in the dense phase. We cannot discard, however, local variations with the local UV field being lower in the northern cut (TMC 1-C) than in the southern cuts TMC1-NH3 and TMC1-CP. As commented above, this is a first guess of the local χ_{UV}. In next section, we will confirm the derived values of χ_{UV} by comparing gas temperatures and chemical abundances with the predictions of the Meudon PDR code.

8.2. Chemical code

We use the steady-state gas-phase Meudon PDR code 1.5.2 (Le Petit et al. 2006; Goicoechea & Le Bourlot 2007; Gonzalez Garcia et al. 2008; Le Bourlot et al. 2012) to estimate the C, O and S elemental abundances. This code computes the steady-state solution to the thermal balance and gas-phase chemical network using accurate radiative transfer calculations and a plane-parallel geometry. The model explicitly considers the H_2 formation on the grain surfaces and adsorption/desorption of H and H_2 from grains. It does not include the accretion/desorption mechanisms for other gas-phase molecules. We assume gas phase elemental abundances below the solar values to take approximately into account depletion effects. The Meudon PDR code uses an extensive gas-phase chemical network which includes the reactions for the ^{13}C and ^{18}O isotologues allowing the direct comparison of chemical predictions with the observed ^{13}CO and $C^{18}O$ column densities.

As a first step, we run a series of models in order to explore the parameter space to determine the values of the cosmic ray ionization rate and elemental abundances that best fit our observations (see Table 5). The adopted physical structure is based on our previous calculations, the "a priori" knowledge of the source (see Ebisawa et al. 2019 and references therein) and the assumption of pressure equilibrium. In practice, we carried out the calculations for an isobaric plane-parallel 30 mag cloud with a constant pressure of 5×10^4 K cm^{-3}, consistent with the physical parameters derived from our observations. Our cloud is illuminated by a UV field, χ_{UV}^{front}, from the front side and $\chi_{UV} = 1$ from the back. We consider two values of χ_{UV}^{front}, $\chi_{UV}^{front} = 10$ and 3, which is the range of values derived in Sect. 8.1. This simple plane-parallel geometry mimics the scenario of a compressed gas layer illuminated from the front proposed by Ebisawa et al. (2019) on the basis of OH 18 cm observations.

Table 5. PDR chemical models.

	ζ_{H_2} (s^{-1})	C/H	C/O	S/H
A	5×10^{-17}	1.38×10^{-4}	0.4	1.5×10^{-5}
B	5×10^{-17}	7.90×10^{-5}	0.4	1.5×10^{-5}
C	5×10^{-17}	3.90×10^{-5}	0.4	1.5×10^{-5}
D	5×10^{-18}	1.38×10^{-4}	0.4	1.5×10^{-5}
E	1×10^{-16}	1.38×10^{-4}	0.4	1.5×10^{-5}
F	5×10^{-17}	1.38×10^{-4}	1.0	1.5×10^{-5}
G	5×10^{-17}	1.38×10^{-4}	0.8	1.5×10^{-5}
H	5×10^{-17}	7.90×10^{-5}	1.0	1.5×10^{-5}
I	5×10^{-17}	7.90×10^{-5}	1.0	8.0×10^{-7}
Best-fit	5×10^{-17}	7.90×10^{-5}	1.0	8.0×10^{-7}

Figure 8 shows the predicted $N(CO)/N(H_2)$, $N(HCO^+)/N(CO)$, $N(CS)/N(H_2)$ and $N(CS)/N(SO)$ ratio as a function of the visual extinction for $\chi_{UV} = 10$, where $N(X)$ is the cumulative column density from 0 to A_V mag of the species X. In general, any line of sight passes through the illuminated cloud surface and the cumulative column density is the parameter directly related with the observed line intensities. In the first column, we show the behavior of the observed abundances under changes in C/H. Here, we compare the predicted cumulative column density N(CO) with the observed column density of $C^{18}O \times 600$ to avoid isotopic fractionation effects. For $A_V > 3$ mag, all the carbon atoms are basically locked in CO and C/H is well determined from the measured CO abundance. Our peak CO abundance, $\sim 1.4 \times 10^{-4}$, shows that even at the low extinction of $A_V = 3$ mag, carbon is depleted by a factor of ~2. Beyond $A_V = 3$ mag, the carbon depletion progressively increases to reach values of ~3 at $A_V \sim 10$ mag.

In the second column, we investigate the chemical effect of varying $\zeta(H_2)$. The value of $\zeta(H_2)$ mainly affects the predicted $N(CS)$ and the $N(HCO^+)/N(CO)$ abundance ratios. The abundance of CS is also dependent on the value of S/H (third column of Fig. 8) which justifies to use $N(HCO^+)/N(CO)$ as a probe of $\zeta(H_2)$. Values of $\zeta(H_2) > (5–10) \times 10^{-17}$ s^{-1} are required to fit the observed values of the $N(HCO^+)/N(CO)$ ratio in TMC 1. The fit is, however, not perfect with several points being over model predictions for all the considered values of $\zeta(H_2)$. We will discuss the value of $\zeta(H_2)$ in more details in Sect. 8.5.

The $N(HCN)/N(CO)$ as well as $N(CS)/N(SO)$ abundance ratios are highly dependent on the C/O gas phase elemental ratio (third column of Fig. 8). We have not been able to fit both ratios with a single C/O value. While the observed $N(HCN)/N(CO)$ is well explained with C/O~0.4, $N(CS)/N(SO)$ points to a value of the C/O ~0.8−1. As commented in Sect. 4.5, the HCN abundance might be underestimated in this moderate density gas. Therefore, we consider that $N(CS)/N(SO)$ is a more reliable tracer of the C/O ratio. We note also that the $N(CS)/N(SO)$ ratio is not very dependent on the S/H value (Col. 4 of Fig. 8) which supports the usage of this ratio to determine C/O. Interestingly, there is not a systematic trend of the $N(CS)/N(SO)$

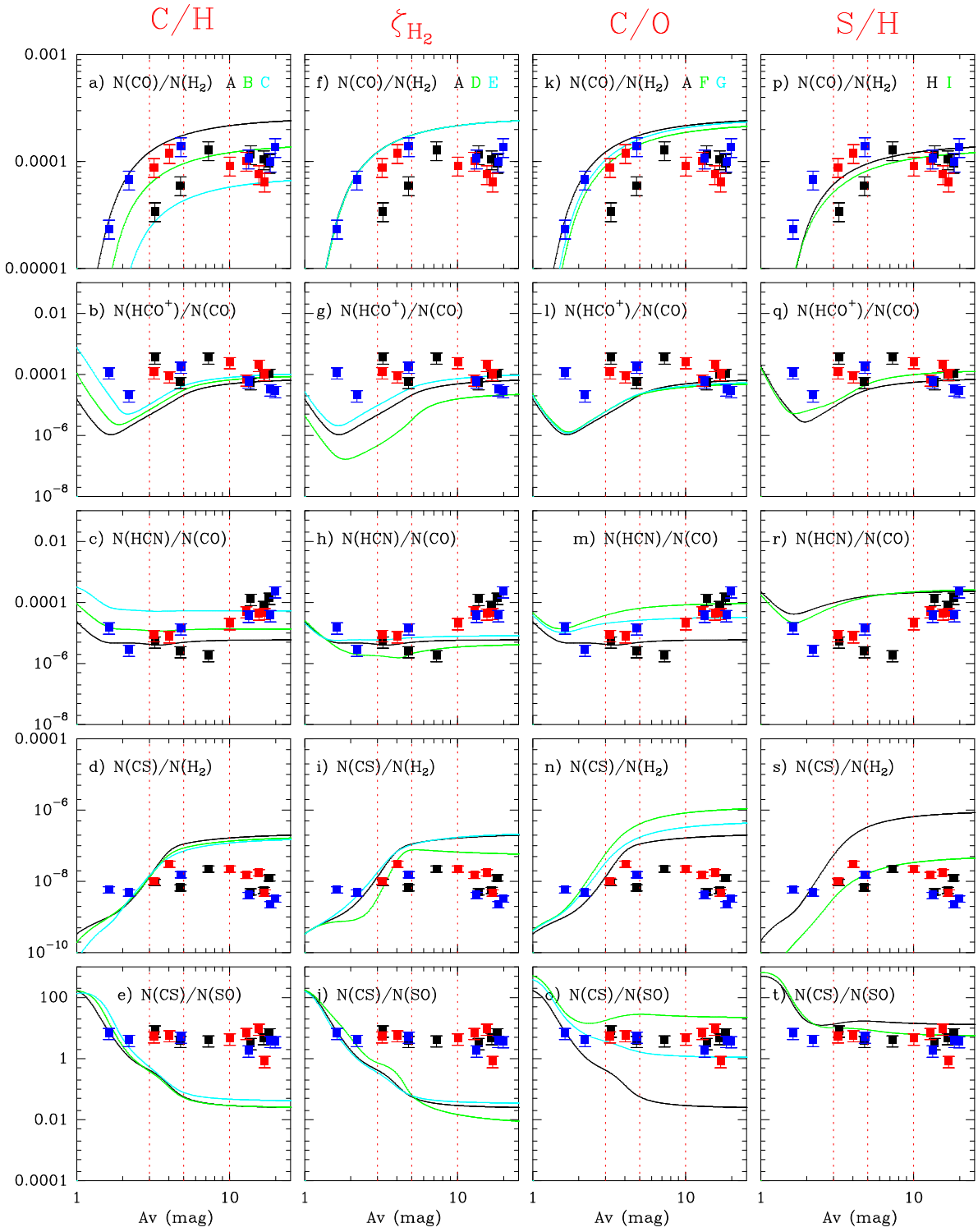

Fig. 8. Comparison between the predictions of models listed in Table 5 and the cumulative column densities derived in TMC 1. In this figure, we have selected N(CO)/N(H_2), N(HCO^+)/N(CO), N(HCN)/N(CO), N(CS)/N(H_2) and N(CS)/N(SO) to explore the parameter space, where N(CO) has been derived from our observations as $N(CO) = 600 \times N(C^{18}O)$ and $N(H_2) = A_V(mag) \times 10^{21}$ cm^{-2}. The observational points are indicated with squares and different colors correspond to the three observed cuts as follows: black for TMC 1-CP, red for TMC 1-NH3 and blue for TMC 1-C. Dashed red lines indicate A_V = 3 mag (C^+/C/CO transition region), A_V = 5 (translucent cloud) and A_V = 10 mag (dense region).

ratio in the translucent cloud that could be identified with a preferential oxygen depletion in this range of visual extinctions. Our data are best fit with C/O~0.8–1. Once the values of $\zeta(H_2)$ and C/O are fixed, the abundances of CS and SO depend almost linearly with S/H (Col. 4). The abundance of CS is well fitted with S/H~8×10^{-7}, i.e., a factor of 20 lower than the solar value, S/H ~1.5×10^{-5}.

Following the analysis described above, we propose that C/H~7.9×10^{-5}, C/O~1 and S/H ~ 8×10^{-7} are the most likely values in the translucent cloud, hereafter our "Best-fit" model.

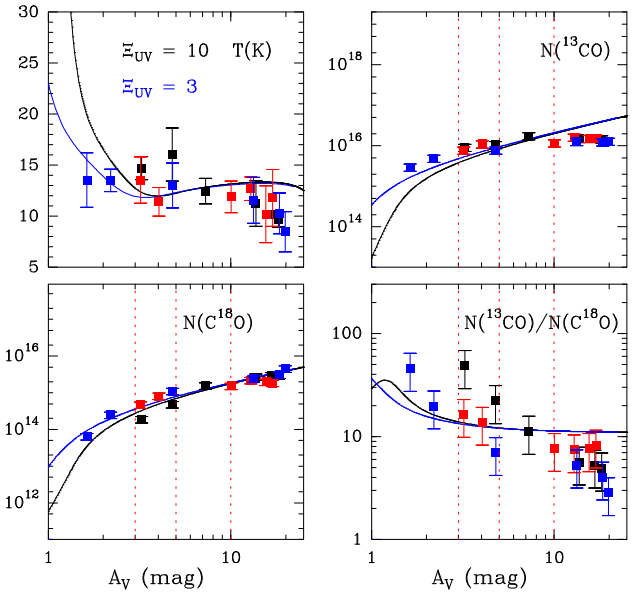

Fig. 9. Comparison between our "Best-fit" model (see Table 5) and the molecular abundances derived in this work. The black line corresponds to the model with χ_{UV}=10 and the blue line to χ_{UV} = 3. Dashed red lines indicate A_V = 3, 5 and 10 mag. The observational points are indicated with squares as in Fig. 8.

In the following we extensively compare this model with our observations.

8.3. C depletion and gas temperature

The gas kinetic temperature is determined by the balance between the heating and cooling processes at a given distance from the cloud border. In molecular clouds, CO is the main coolant and carbon depletion is determining the gas temperature. The CO lines are optically thick even at moderate visual extinctions and the CO line profiles usually present self-absorption features. For this reason, we have used the rarer isotopologue $C^{18}O$ to estimate the total CO column density by assuming a fixed $N(^{12}CO)/N(C^{18}O)$ ratio. The CO abundances thus obtained were used to compare with observations in Fig. 8.

The Meudon PDR code computes the abundances of CO, ^{13}CO and $C^{18}O$ taking into account the self-shielding effects for ^{12}CO and ^{13}CO, and the effects of the possible overlap between H, H_2, CO and ^{13}CO UV transitions, as well as the isotopic fractionation reactions. Here, we directly compare the predicted ^{13}CO and $C^{18}O$ abundances with observations. In Fig. 9 we show our "Best-fit" model with χ_{UV} = 10 (black) and χ_{UV} = 3 (blue) predictions with the observed ^{13}CO and $C^{18}O$ column densities. For further comparison, we also plot the gas temperature as computed by the Meudon code. We find quite good agreement of the observed T_{gas} and $N(C^{18}O)$ in the TMC 1-CP and TMC 1-NH3 cuts for χ_{UV} = 10. In these cuts, we do not have any observed position with A_V < 3 mag. On the other hand, the gas kinetic temperature in the cut across TMC 1-C are better fitted with χ_{UV} = 3. These results support the interpretation of a lower UV field in the northern part of the filament than towards the south. In this plot we also represent $N(^{13}CO)$ and the $N(^{13}CO)/N(C^{18}O)$ ratio as a function of the visual extinction from the cloud border. Although we have a good qualitative agreement between the derived $N(^{13}CO)$ and observations, the model underestimates $N(^{13}CO)$ in the outer A_V < 5 mag. We consider that this disagreement is due to the fact that, at these low visual extinctions, $N(^{13}CO)$ is very sensitive to the uncertainties in the UV illuminating field and the detailed cloud geometry.

8.4. Depletions of O and S

The determination of the O and S depletions is very likely the most challenging part of this project. The main oxygen reservoirs, O, H_2O and OH, cannot be observed in the millimeter domain and oxygen depletion has to be derived indirectly from the C/O ratio. As commented above N(HCN)/N(CO) and N(CS)/N(SO) are good tracers of the C/O ratio. Since we have problems to account for observed abundances of HCN and N_2H^+, we prefer to use N(CS)/N(SO) as a proxy of the C/O ratio.

Atomic S in the outer layers of the cloud and solid-H_2S in the dense cores are predicted to be the main sulfur reservoirs and both of them are difficult to observe. Thus, we need to derive the S abundance indirectly by observing minor sulfur compounds. The most abundant easily observable S-species in gas phase are CS, SO and H_2S. Out of them, only CS and SO are thought to be formed in gas phase while the formation of H_2S is only understood as the product of the hydrogenation of S on the grain surfaces. Our team has been working in improving the sulfur chemical network by revising the rates of important reactions in the CS and SO chemistry at low temperatures. Fuente et al. (2016) already presented calculations of the S + O_2 → SO + O rate at temperatures < 50 K. In this paper, we include new calculations of the SO + OH → SO_2 + O reaction rate for temperatures below 300 K (see Appendix A). These new rates have been included in the gas-phase chemical network used by the Meudon code to obtain the most accurate determination of the amount of sulfur in gas phase. Figure 10 shows the comparison of the CS, SO, HCS^+, HCN and N_2H^+ column densities with model predictions. We have a fair agreement for all the species except for the N-bearing compounds HCN and N_2H^+ using C/O = 1 and S/H = 8×10^{-7}. We also include HCS^+ in our comparison although we have very few detections of this species in the translucent phase.

8.5. Gas ionization fraction, X(e^-)

The gas ionization fraction determines the coupling of the gas dynamics with the magnetic field and it is, therefore, a key parameter in star formation studies. At the scale of the molecular cloud, UV photons and cosmic rays are the main ionization agents in the diffuse/translucent phase, and carbon and sulfur are the main electron donors. At the scale of protostellar disk formation, the dust is the main contributor to the magneto-hydrodynamics resistivity. In the following, we discuss the uncertainties in our estimate of X(e^-) and the implications of our results in this context.

Over the past three decades, several attempts have been carried out to estimate ζ_{H_2} in dense cores from measurements of the abundances of various chemical species (see compilation by Padovani et al. 2009). The values of ζ_{H_2} derived by Caselli et al. (1998) through DCO^+ and HCO^+ abundance ratios span a range of about two orders of magnitudes from $\sim 10^{-17}$ to $\sim 10^{-15}$ s^{-1}. This large scatter may reflect intrinsic variations of the cosmic rays flux from core to core but, as discussed by the authors, might be the consequence of the sensitivity of the results to several model assumptions, mainly the value of specific chemical reaction rates and elemental depletions. In order to minimize these uncertainties, Fuente et al. (2016) used a gas-phase chemical model to fit the abundances of 22 neutral and ionic species

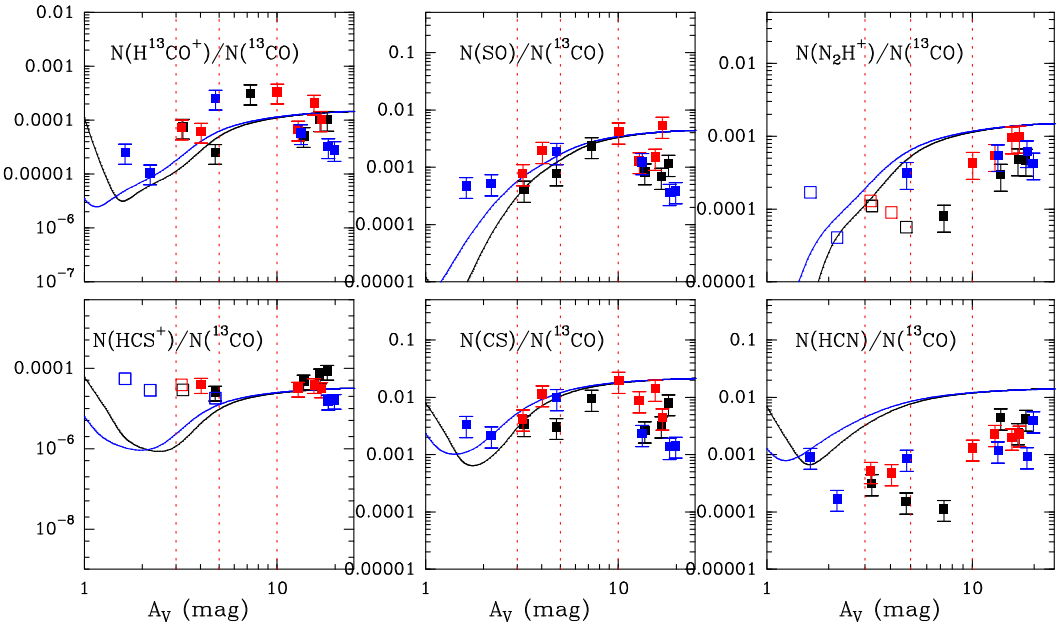

Fig. 10. Comparison between our "Best-fit" model (see Table 5) and the molecular abundances derived in this work. The black line corresponds to the model with $\chi_{UV} = 10$ and the blue line to $\chi_{UV} = 3$. Dashed red lines indicate $A_V = 3$, 5 and 10 mag. The observational points are indicated with squares as in Fig. 8.

in order to determine the local value of the cosmic ray ionization rate together with the depletion factors towards Barnard 1b. They estimated a value of ζ_{H_2} between 3×10^{-17} and 10^{-16} s^{-1}, i.e., an uncertainty of a factor of 4.

Several works have been dedicated to estimate ζ_{H_2} in diffuse clouds. The discovery of significant abundances of H_3^+ in diffuse clouds by McCall et al. (1998) led to values of $\zeta_{H_2} > 2 \times 10^{-16}$ s^{-1}. Given the simplicity of H_3^+ chemistry, this value was widely accepted as considered more reliable than previous estimates. Neufeld et al. (2010) found $\zeta_{H_2} \approx 1.2$–4.8×10^{-16} s^{-1} from observations of OH^+ and H_2O^+in clouds with low molecular fraction. A recent comprehensive work by Neufeld & Wolfire (2017) established that the ionization rate per H_2 in diffuse molecular gas is $\zeta_{H_2} = (5.3 \pm 1.1) \times 10^{-16}$ s^{-1}.

In this work we have estimated the elemental abundances and X(e$^-$) in the translucent part of TMC 1. Our observations highlight the low-density (approximately a few 10^3 cm^{-3}) cloud envelope, i.e., the transition from the diffuse medium to the dense cores. In the translucent envelope where most of the carbon is already in molecular form, X(e$^-$) is mainly dependent on ζ_{H_2} and the elemental abundance of S. In order to obtain the range of values of ζ_{H_2} and S/H consistent with our observations we have run a grid of models with ζ_{H_2} = (1, 5.1, 8.6, 14.4, 24.4) $\times 10^{-16}$ s^{-1} and S/H = (0.01, 0.018, 0.058, 0.10, 0.19, 0.34, 0.61 and 1.1) $\times 10^{-5}$. All the other parameters are fixed to the values in the "Best-fit" model and $\chi_{UV} = 3$. We select the model predictions and observations at $A_V = 5$ mag, as representative of the translucent phase. From our observations, we have derived values of $N(HCO^+)/N(CO) = 0.2$–2.7×10^{-4} at this visual extinction (see Fig. 11). Values of $N(HCO^+)/N(CO) > 1.3 \times 10^{-4}$ cannot be fitted with our grid of models (see Fig. 11). It is noticeable that an increase of ζ_{H_2} of a factor of 10, from $\sim 3 \times 10^{-17}$ to $\sim 2.2 \times 10^{-16}$ s^{-1}, only produces an increase of a factor of ~2–3, from $\sim 5 \times 10^{-5}$ to $\sim 1.2 \times 10^{-4}$, in the predicted $N(HCO^+)/N(CO)$ ratio which makes it very difficult to estimate the value of ζ_{H_2} with an accuracy better than a factor of 10 based only on the $N(HCO^+)/N(CO)$ ratio. To further constrain the values of ζ_{H_2} and S/H, we have tried to fit X(CS) and $N(CS)/N(SO)$ ratio, as well. The range of the observed values of $N(CS)/N(SO)$ is of ~4 to 8 which is best fitted with ζ_{H_2} of ~ 0.5–1.8×10^{-16} s^{-1} and S/H ~ 0.4–2.2×10^{-6} (see Fig. 11). Taking all into account, we conclude that $\zeta_{H_2} = 0.5$–1.8×10^{-16} s^{-1} in the TMC 1 translucent envelope. This value is similar to that found by Fuente et al. (2016) in Barnard 1b and it is within the range of the values obtained by Caselli et al. (1998) in dark cores. It is also consistent with the accepted value in diffuse clouds (McCall et al. 1998; Neufeld et al. 2010). Therefore, we do not add any evidence of variation of ζ_{H_2} within a factor of 3.

It is also interesting to find the relationship between ζ_{H_2} and X(e$^-$), that is dependent on the local density and the elemental abundances. With the physical and chemical conditions derived in the studied region, we need S/H $= 0.04$–0.2×10^{-5} to account for the measured CS abundance (see Fig. 11a). As shown in Fig. 11, this would imply that X(e$^-$) $\sim 9.8 \times 10^{-8}$–3.6×10^{-7} in the transition from the diffuse to the dense medium in TMC 1.

9. Dense phase

In the following, we carry out a phenomenological analysis of the chemical changes observed across the cuts in the dense phase. The abundance of most molecules decreases with the visual extinction from $A_V = 10$ to ~20 mag. In Table 6 we show the estimated molecular abundances and the values of R_{TD}(X), defined as the ratio between the abundance of the species X in the translucent phase (red lines in Figs. 5 and 6) over the abundance towards each cut extinction peak [offset (0″,0″)]. Values of R_{TD}(CO), $R_{TD}(HCO^+)$, R_{TD}(CS) and R_{TD}(SO) >1 are found in the three studied cuts. We cannot derive any conclusion, however, on HCS^+ with very few detections in the translucent phase and an abundance a factor of ~4 larger towards TMC 1-CP than towards the TMC 1-NH3 and TMC1-C. The value of $R_{TD}(HCO^+)$ is very dependent on the CO depletion and the change in the gas ionization fraction in the higher density core center, X(e$^-$) $\propto \sqrt{\zeta_{H_2}/n}$. The variations in the CO, CS and SO abundances are better understood as the consequence of the freeze-out of S- and O-bearing molecules onto the grain mantles.

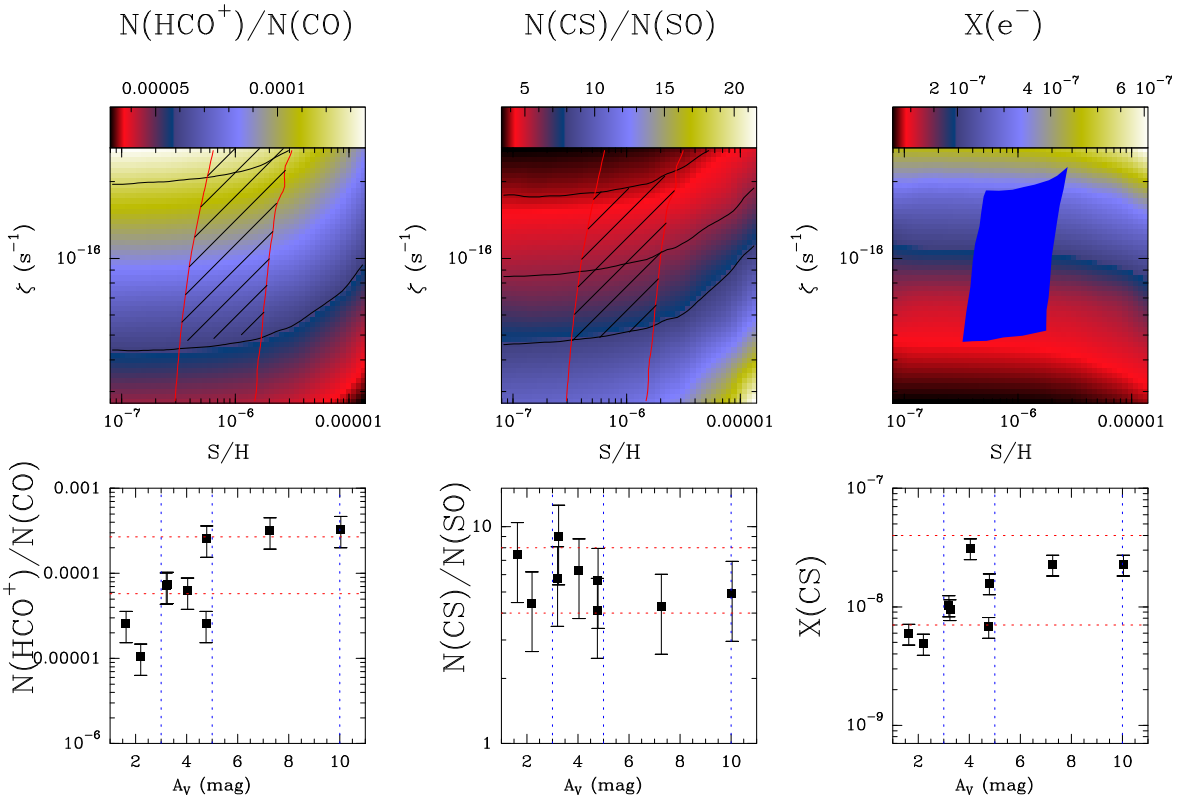

Fig. 11. *Left*: the color map shows the $N(HCO^+)/N(CO)$ ratio as a function of ζ_{H_2} and S/H. Black contours correspond to $N(HCO^+)/N(CO) = 5.8\times10^{-5}$ and 1.2×10^{-4}. Red contours indicate $X(CS) = 1\times10^{-8}$ and 4×10^{-8}, which is the range of CS abundances derived in the translucent part. *Center*: the color map shows the N(CS)/N(SO) ratio as a function of ζ_{H_2} and S/H. Contours are N(CS)/N(SO) = 4, 5.8 and 8. Red contours are the same as in the left panel. *Right*: gas ionization fraction, $X(e^-) = n(e^-)/n_H$, as a function of ζ_{H_2} and S/H. According with our data, the blue region marks the range of values expected in the translucent part of TMC 1. *Bottom panels*: observed values in the translucent cloud. Dashed red lines are: 5.8×10^{-5} and 2.7×10^{-4} in the $N(HCO^+)/N(CO)$ panel; 4 and 8 in the N(CS)/N(SO) panel and 7×10^{-9} and 4×10^{-8} in the X(CS) panel.

The depletions of these molecules are slightly higher towards TMC 1-C than towards TMC 1-NH3 and TMC1-CP, suggesting a different density structure and/or a more evolved chemical state for the former.

10. Gas chemical composition from the diffuse to the translucent phase

In general we refer to the gas with densities of $n_H < 100\,cm^{-3}$ and $T_k \sim 100$ K as diffuse gas. In this phase, the gas is partially atomic and CO is not a good tracer of the total mass of molecular gas. The molecular content of the diffuse gas has been determined by a series of studies based on the molecular absorption lines at millimeter wavelengths which revealed a surprisingly rich chemistry (see Liszt et al. 2018 and references therein). Translucent clouds are characterized by $n_H \sim$ a few $1000\,cm^{-3}$, $T_k \sim 20$–30 K, the gas is mostly in molecular form and CO is a good mass tracer. The higher densities of this phase permit the detection of low-excitation molecular emission lines. Although difficult, the comparison of the chemical composition of the diffuse and translucent phases might provide important clues for the understanding of the chemical evolution of the gas in the interstellar medium. All the species studied in this paper, except N_2H^+, have been detected in the diffuse gas. Interestingly, we have only one detection of N_2H^+ at $A_V \sim 5$ mag with $N(N_2H^+)/N(HCO^+) \sim 0.02$. Liszt & Lucas (2001) measured $N(N_2H^+)/N(HCO^+) < 0.002$ towards 3C111. This quasar is actually seen through a small hole (region of lower than average extinction) in an outlying cloud in the Taurus cloud complex (Lucas & Liszt 1998) and hence $A_V \sim 5$ mag can be considered as a threshold for the N_2H^+ detection in Taurus.

In Fig. 12 we show the comparison of the abundances with respect to H_2 of the studied molecules with those from our survey. There is a large dispersion in the plot of the molecular abundances as a function of the visual extinction. We recall that diffuse clouds are not only characterized by low values of the visual extinction but also for low hydrogen densities. In addition, in the diffuse gas, with several clouds along the line of sight, the visual extinction is not necessarily related to the local UV field. One can find a better correlation if one considers the abundances versus the local density and assumes that in the diffuse gas the local density is around 50–100 cm^{-3}. For HCO^+, SO and CS we find a trend with their abundances increasing with density from the diffuse to the translucent phase. All these molecules present their peak abundances in the translucent region. HCN might be the one exception to this rule with lower abundances in the translucent phase than in the diffuse gas. As discussed above, the HCN column densities might be severely underestimated in the translucent cloud. It is also interesting the case of HCS^+ which was detected in the diffuse medium by Lucas & Liszt (2002) with an abundance ratio $X(CS)/X(HCS^+) \sim 13 \pm 1$ that is ~40 times lower than the value of $X(CS)/X(HCS^+) \sim 400$ we have measured in the translucent cloud. This unveils a different formation path of CS in diffuse (dissociative recombination of HCS^+) and translucent ($SO + C \rightarrow CS + O$) clouds.

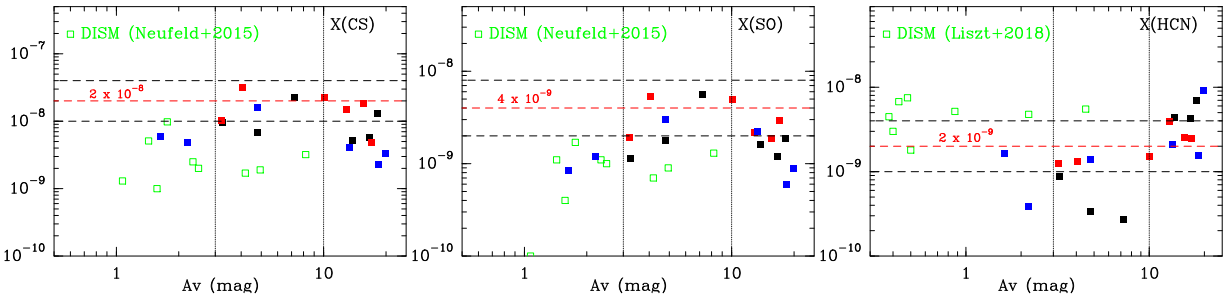

Fig. 12. Comparison between the abundances in TMC 1 with those observed in the diffuse gas by Neufeld et al. (2015) and Liszt et al. (2018).

Table 6. Molecular abundances and depletions in TMC 1.

Mol	TMC 1-CP	TMC 1-NH3	TMC 1-C
X(CO)	9.7×10^{-5}	6.5×10^{-5}	1.4×10^{-4}
X(HCO^+)	1.0×10^{-8}	6.7×10^{-9}	3.9×10^{-9}
X(HCN)	7.0×10^{-9}	2.4×10^{-9}	9.0×10^{-9}
X(CS)	1.3×10^{-8}	4.8×10^{-9}	3.3×10^{-9}
X(SO)	1.8×10^{-9}	2.9×10^{-9}	8.8×10^{-10}
X(HCS^+)	1.4×10^{-10}	3.3×10^{-11}	3.6×10^{-11}
X(N_2H^+)	7.7×10^{-10}	1.0×10^{-9}	9.6×10^{-10}
R_{TD}(CO)	1.7	2.6	1.2
R_{TD}(HCO^+)	1.3	1.9	3.3
R_{TD}(HCN)	0.1	0.4	0.1
R_{TD}(CS)	1.5	4.2	6.0
R_{TD}(SO)	2.2	1.4	4.5
R_{TD}(HCS^+)	0.3	1.5	<1
R_{TD}(N_2H^+)	<0.8	<0.6	<0.6

Notes. Molecular abundances with respect to H_2 towards the (0″,0″) positions of TMC 1-CP, TMC 1-NH3 and TMC 1-C. R_{TD}(X) is the ratio between the abundance of the species X in the translucent phase (red lines in Figs. 5 and 6) over the abundance towards each cut extinction peak [i.e., offset (0″,0″)].

11. Elemental depletions and grain growth

The depletion of an element X in the ISM is defined in terms of its reduction factor below the expected abundance relative to that of hydrogen if all of the atoms were in the gas phase,

$$[\mathrm{Xgas/H}] = \log N(\mathrm{X})/N(\mathrm{H}) - \log(\mathrm{X/H})_\odot. \quad (2)$$

In this expression, N(X) is the column density of element X and N(H) represents the column density of hydrogen in both atomic and molecular form, i.e., N(H I) + $2N(H_2)$. The missing atoms of element X are presumed to be locked up in solids within dust grains or in the icy mantle. In the diffuse gas, atomic absorption lines can be used to determine abundances by comparison with the atomic and molecular hydrogen column densities measured through Lyman alpha and Lyman–Werner transitions. Jenkins (2009) presents a comprehensive study of the elemental depletions in diffuse clouds. In general, depletions increase with the average density along the line of sight. However, depletions are observed to vary from one line of sight to another. Savage & Sembach (1996) interpreted these variations in terms of averages of warm (presumably low density) gas and cool (denser) gas. In his review, Jenkins (2009) distinguishes between two cases, "minimum" and "maximum" depletion to characterize the range of these variations in diffuse clouds.

In Table 7 we compare our estimates in the translucent part of TMC1 with the "minimum" and "maximum" depletion cases, in diffuse clouds. Our value of C/H is consistent within a factor of 2 with the "maximum" depletion diffuse case. A significant difference is found, however, in the O and S depletions which are ∼4 times larger in the translucent phase than in the "maximum" depletion case. Although we observe a smooth increase in the C and O depletions with visual extinction in the translucent phase, the C/O ratio remains quite constant (∼1). The scatter in the measured X(CS)/X(SO) values can hinder a smooth variation in the derived C/O value but an almost constant C/O ratio can be understood if the freeze-out of CO is the main process that changes the grain composition in this region. Regarding sulfur, we measure a depletion factor of ∼7–40 in the translucent cloud. Although some authors like Jenkins (2009) casts doubts on this interpretation, it is widely accepted that sulfur is not depleted in diffuse clouds (see also Neufeld et al. 2015). Adopting this scenario, sulfur atoms (or ions) should be massively incorporated to dust grains from the HI/H_2 ($A_V \sim 1$) to the C^+/C/CO transition phases to explain a depletion factor of ∼7–40 in the translucent medium.

In Table 7 we also compare the depletions estimated in the translucent part of TMC 1 with the chemical composition towards TMC 1-CP. We have estimated the C and O depletions from the CO abundance reported by Agúndez & Wakelam (2013) and assumed C/O ∼ 1. The S depletion is based on recent results of Vidal et al. (2017). While C and O depletions agree within a factor of 2 with the values in the translucent cloud, sulfur depletion needs to be increased by at least a factor 10 (depletion of ∼200 compared to solar) to account for the observed abundances of S-bearing molecules.

Following these findings, we propose that two strong S depletion events should occur across the cloud. The first occurs in the transition from the diffuse to the translucent phase. In this transition, ∼90% of the sulfur is incorporated into dust grains while ∼10% is hidden as atomic sulfur in the gas phase. The second strong depletion occurs in the dense gas where a thick ice mantle is formed on the grain surfaces (see the illustrative scheme in Fig. 13). The exact composition of the icy mantle has not established yet. For large values of C/O and early times, atomic sulfur would remain as the main sulfur reservoir in the dense gas. These S atoms would become adsorbed on the icy surface, and would react with hydrogen atoms to produce solid HS and H_2S in ices. These latest reservoirs are supported by observations from the comet 67P with Rosetta showing that H_2S is the most important S-bearing species in cometary ices (Calmonte et al. 2016). For low C/O ratios and close to the steady state, chemical models predict that most sulfur is in molecular form as SO and SO_2. These molecules are rapidly frozen onto dust grains at high densities and temperatures below ∼50 K (see, e.g., Pacheco-Vázquez et al. 2016), trapping the sulfur in the solid phase. Observationally, OCS is the only S-bearing molecule unambiguously detected in ice mantles because of its large band strength in the

Table 7. Elemental gas phase abundances.

	Solar [a]	$DIFF_{min}$ [b]	$DIFF_{max}$ [c]	TRANSLUCENT [d]	TMC 1-CP [e]	Orion KL [f]	L1157-B1 [g]
C/H	2.88×10^{-4}	2.20×10^{-4}	1.76×10^{-4}	8.00×10^{-5}	9.00×10^{-5}	1.79×10^{-4}	1.79×10^{-4}
O/H	5.75×10^{-4}	5.50×10^{-4}	3.34×10^{-4}	8.00×10^{-5}	6.40×10^{-5}	4.45×10^{-4}	4.45×10^{-4}
S/H	1.50×10^{-5}	1.25×10^{-5}	3.50×10^{-6}	8.00×10^{-7}	$<8.00\times10^{-8}$	1.43×10^{-6}	6.00×10^{-7}

References. [a]Lodders et al. (2003); [b]minimum depletion case of Jenkins (2009); [c]maximum depletion case of Jenkins (2009); [d]this work; [e]Agúndez & Wakelam (2013); Vidal et al. (2017); [f]Esplugues et al. (2014); [g]Holdship et al. (2016).

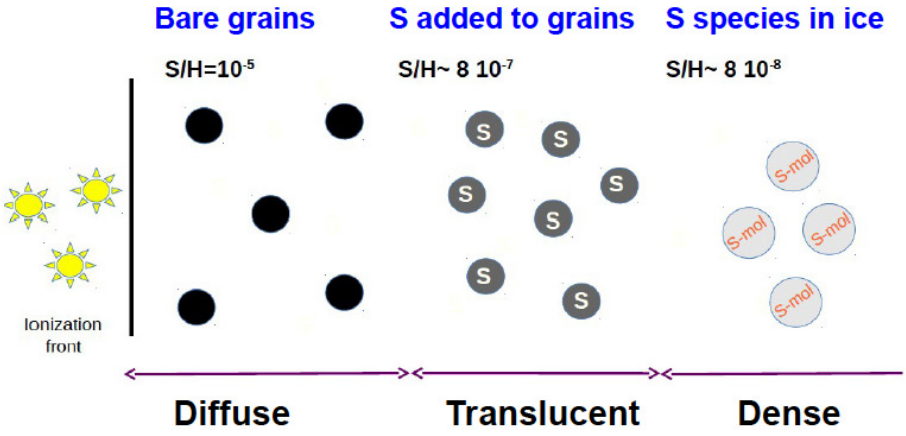

Fig. 13. Scheme of the proposed scenario of the sulfur gas-phase/solid state evolution in TMC 1 (courtesy of S. Cazaux).

infrared (Palumbo et al. 1995) and, tentatively, SO_2 (Boogert et al. 1997). H_2S has not been detected in interstellar ices through infrared absorption experiments (Jiménez-Escobar & Muñoz Caro 2011).

Regardless of the exact chemical composition, the sulfur budget in the ice is expected to return to the gas phase in hot cores and bipolar outflows. The study of the sulfur chemistry in these environments can therefore provide some clues on the fate of sulfur. In Table 7, we show the values of sulfur depletion derived towards the hot core Orion KL (Esplugues et al. 2014) and the shocked region L1157-B1 (Holdship et al. 2016). Interestingly, the sulfur depletion in these two sources is ~10–30 relative to the solar value, i.e., similar to the value we measured in the translucent phase. A similar value of sulfur depletion was measured in bipolar outflows by Anderson et al. (2013) using observations of the infrared space telescope *Spitzer*. This suggests that the fraction of sulfur incorporated onto the grains in the diffuse-translucent transition (~90%) is not released to the gas phase when the icy mantles are destroyed. This has important implications for star and planet formation studies. During the formation of a low-mass star, the grain cores are not destroyed except in the bow shocks formed at the tip of high-velocity jets. If our hypothesis is correct, 90% of the S atoms would remain locked in the grains in the inner regions of protoplanetary disks where planet formation occurs.

12. Summary and conclusions

This paper is based on the GEMS (GEMS, PI: A. Fuente) of the prototypical dark cloud TMC 1. The TMC is one of the closest, low-mass star-forming regions at 140 pc. In this paper we investigate the chemistry to derive the elemental gas-phase abundances and the gas ionization fraction in the translucent part (A_V < 10 mag) of this molecular cloud. The chemistry in this transition from the diffuse to the dense gas determines the initial conditions for the formation of the dense contracting cores.

- We use millimeter observations of a selected sample of species carried out with the IRAM 30 m telescope (3 and 2 mm) and the 40 m Yebes telescope (1.3 cm and 7 mm) to determine the fractional abundances of CO, HCO^+, HCN, CS, SO, HCS^+ and N_2H^+ in positions along three cuts intersecting the main filament at positions TMC 1-CP, TMC 1-NH3 and TMC 1-C over which the visual extinction varies between peak values of $A_V \sim 20$ and 3 mag.
- None of the studied molecules presents constant abundance across the studied cuts. According to their variations with visual extinction, we can differentiate three groups. The first group is formed by the abundant molecule ^{13}CO. This molecule reaches its peak value at $A_V \sim 3$ mag and then progressively decreases with visual extinction. The second group is formed by HCO^+, CS and SO; the abundances of these molecules increases with visual extinction until $A_V \sim 5$ mag where they present a narrow peak and then progressively decreases towards the extinction peak. In the third group, the abundance of the N-bearing molecules HCN and N_2H^+ increases from $A_V \sim 3$ mag until the extinctions peaks at $A_V \sim 20$ mag.
- By comparison of the molecular abundances with the Meudon PDR code, we derive the C, O and S elemental depletions, and hence the gas ionization degree as a function of the visual extinction at each position. Our data show that even at $A_V \sim 3$–4 mag where the transition C^+/C/CO occurs, significant depletions of C, O and S are found. In fact, C/H varies between $\sim8\times10^{-5}$ and $\sim4\times10^{-5}$ in the translucent cloud ($3 < A_V < 10$ mag). Moreover, the C/O ratio is ~0.8–1, suggesting that the O is preferentially depleted in the diffuse phase ($A_V < 3$ mag). Regarding sulfur, we estimate S/H ~0.4–2.2×10^{-6} in this moderately dense region.
- The detailed modeling of the chemistry in the translucent phase and our estimate of the elemental abundances allow us to constrain the value of ζ_{H_2} to ~0.5–1.8×10^{-16} s^{-1}. This value is slightly lower (a factor of ~3) than that derived by

Neufeld & Wolfire (2017), $\zeta_{H_2} = (5.3 \pm 1.1) \times 10^{-16}$ s^{-1}, in the diffuse medium.

Based on our results, we propose that the freeze out of CO is the main process that changes the grain composition in the translucent part of the cloud producing a progressive depletion of C and O from $A_V \sim 3$ mag to $A_V \sim 10$ mag. Regarding sulfur, we measure a constant depletion of ∼7−40 across the translucent cloud. This suggests that sulfur atoms (or ions) would have been massively incorporated onto dust grains from the HI/H_2 ($A_V \sim 1$) to the C^+/C/CO transition to reach a depletion of ∼7–40 in the translucent medium. In order to account for the chemical composition in the TMC 1-CP core, a second strong S depletion should occur in the dense cloud. Interestingly, the S atoms incorporated into grains during the diffuse and translucent phase are not returned back to the gas phase during the formation of a low-mass star.

Acknowledgements. We thank the Spanish MINECO for funding support from AYA2016-75066-C2-1/2-P, and the ERC under ERC-2013-SyG, G. A. 610256 NANOCOSMOS. J.M. acknowledges the support of ERC-2015-STG No. 679852 RADFEEDBACK. S.P.T.M. acknowledges to the European Union's Horizon 2020 research and innovation program for funding support given under grant agreement No 639459 (PROMISE). R.M.D. acknowledges support provided by an award from the Simons Foundation (SCOL#321183, KO). G.M.C. acknowledges funding support fromAYA2017-85322-R. M.T. acknowledges partial support from project AYA2016-79006-P.

References

Agúndez, M., & Wakelam, V. 2013, Chem. Rev., 113, 8710
Alonso-Albi, T., Fuente, A., Crimier, N., et al. 2010, A&A, 518, A52
Anderson, D. E., Bergin, E. A., Maret, S., & Wakelam, V. 2013, ApJ, 779, 141
André, P., Men'shchikov, A., Bontemps, S., et al. 2010, A&A, 518, L102
Bacmann, A., Lefloch, B., Ceccarelli, C., et al. 2002, A&A, 389, L6
Ballester, M. Y., & Varandas, A. J. C. 2005, PCCP, 7, 2305
Ballester, M. Y., & Varandas, A. J. C. 2007, Chem. Phys. Lett., 422, 279
Ballester, M. Y., Orozco-Gonzalez, Y., Garrido, J. D., & Santos, H. F. D. 2010, J. Chem. Phys., 132, 044310
Beckwith, S. V. W., Sargent, A. I., Chini, R. S., & Guesten, R. 1990, AJ, 99, 924
Ben Abdallah, D., Najar, F., Jaidane, N., Dumouchel, F., & Lique, F. 2012, MNRAS, 419, 2441
Bernard, J.-P., Paradis, D., Marshall, D. J., et al. 2010, A&A, 518, L88
Blitz, M. A., McKee, K. W., & Pilling, M. J. 2000, Proc. Combust. Inst., 28, 2491
Bockelée-Morvan, D., Lis, D. C., Wink, J. E., et al. 2000, A&A, 353, 1101
Boogert, A. C. A., Schutte, W. A., Helmich, F. P., Tielens, A. G. G. M., & Wooden, D. H. 1997, A&A, 317, 929
Bron, E., Daudon, C., Pety, J., et al. 2018, A&A, 610, A12
Calmonte, U., Altwegg, K., Balsiger, H., et al. 2016, MNRAS, 462, S253
Cambrésy, L. 1999, A&A, 345, 965
Caselli, P., Walmsley, C. M., Terzieva, R., & Herbst, E. 1998, ApJ, 499, 234
Caselli, P., Walmsley, C. M., Tafalla, M., Dore, L., & Myers, P. C. 1999, ApJ, 523, L165
Caselli, P., Walmsley, C. M., Zucconi, A., et al. 2002, ApJ, 565, 344
Cernicharo, J., & Guelin, M. 1987, A&A, 176, 299
Daniel, F., Faure, A., Pagani, L., et al. 2016, A&A, 592, A45
Denis-Alpizar, O., Stoecklin, T., Guilloteau, S., & Dutrey, A. 2018, MNRAS, 478, 1811
Dobashi, K., Shimoikura, T., Nakamura, F., et al. 2018, ApJ, 864, 82
Dorta-Urra, A., Zanchet, A., Roncero, O., & Aguado, A. 2015, J. Chem. Phys., 142, 154301
Ebisawa, Y., Sakai, N., Menten, K. M., & Yamamoto, S. 2019, ApJ, 871, 89
Elias, J. H. 1978, ApJ, 224, 857
Esplugues, G. B., Viti, S., Goicoechea, J. R., & Cernicharo, J. 2014, A&A, 567, A95
Fair, R. W., & Thrush, B. A. 1969, Trans. Faraday Soc., 65, 1557
Fehér, O., Tóth, L. V., Ward-Thompson, D., et al. 2016, A&A, 590, A75
Flower, D. R. 1999, MNRAS, 305, 651
Foreman-Mackey, D., Hogg, D. W., Lang, D., & Goodman, J. 2013, PASP, 125, 306
Friesen, R. K., Pineda, J. E., Rosolowsky, E., et al. 2017, ApJ, 843, 63
Fuente, A., Cernicharo, J., Roueff, E., et al. 2016, A&A, 593, A94
Garrod, R. T., & Pauly, T. 2011, ApJ, 735, 15
Goicoechea, J. R., & Le Bourlot, J. 2007, A&A, 467, 1
Goicoechea, J. R., Pety, J., Gerin, M., et al. 2006, A&A, 456, 565
Goldsmith, P. F., Heyer, M., Narayanan, G., et al. 2008, ApJ, 680, 428
Gonzalez-Alfonso, E., & Cernicharo, J. 1993, A&A, 279, 506
Gonzalez Garcia, M., Le Bourlot, J., Le Petit, F., & Roueff, E. 2008, A&A, 485, 127
Goodman, J., & Weare, J. 2010, Commun. Appl. Math. Comput. Sci., 5, 65
Gratier, P., Majumdar, L., Ohishi, M., et al. 2016, ApJS, 225, 25
Griffin, M. J., Abergel, A., Abreu, A., et al. 2010, A&A, 518, L3
Grozdanov, T. P., & Solov'ev, E. A. 1982, J. Phys. B, 15, 1195
Hernandez, A. K., Tan, J. C., Caselli, P., et al. 2011, ApJ, 738, 11
Hocuk, S., Szűcs, L., Caselli, P., et al. 2017, A&A, 604, A58
Holdship, J., Viti, S., Jimenez-Serra, I., et al. 2016, MNRAS, 463, 802
Hollenbach, D. J., Takahashi, T., & Tielens, A. G. G. M. 1991, ApJ, 377, 192
Jenkins, E. B. 2009, ApJ, 700, 1299
Jiménez-Escobar, A., & Muñoz Caro, G. M. 2011, A&A, 536, A91
Johnson, B. R. 1987, J. Chem. Phys., 86, 1445
Jourdain, J. L., Bras, G. L., & Combourieu, J. 1979, Int. J. Chem. Kinet., 11, 569
Kirk, J. M., Ward-Thompson, D., Palmeirim, P., et al. 2013, MNRAS, 432, 1424
Kramer, C., Alves, J., Lada, C. J., et al. 1999, A&A, 342, 257
Le Bourlot, J., Le Petit, F., Pinto, C., Roueff, E., & Roy, F. 2012, A&A, 541, A76
Le Petit, F., Nehmé, C., Le Bourlot, J., & Roueff, E. 2006, ApJS, 164, 506
Lippok, N., Launhardt, R., Semenov, D., et al. 2013, A&A, 560, A41
Lique, F., & Spielfiedel, A. 2007, A&A, 462, 1179
Lique, F., Cernicharo, J., & Cox, P. 2006a, ApJ, 653, 1342
Lique, F., Spielfiedel, A., & Cernicharo, J. 2006b, A&A, 451, 1125
Liszt, H., & Lucas, R. 1996, A&A, 314, 917
Liszt, H., & Lucas, R. 2001, A&A, 370, 576
Liszt, H., Gerin, M., Beasley, A., & Pety, J. 2018, ApJ, 856, 151
Loison, J.-C., Wakelam, V., & Hickson, K. M. 2014, MNRAS, 443, 398
Lucas, R., & Liszt, H. 1998, A&A, 337, 246
Lucas, R., & Liszt, H. S. 2002, A&A, 384, 1054
Malinen, J., Juvela, M., Rawlings, M. G., et al. 2012, A&A, 544, A50
Maret, S., Bergin, E. A., & Tafalla, M. 2013, A&A, 559, A53
McCall, B. J., Geballe, T. R., Hinkle, K. H., & Oka, T. 1998, BAAS, 30, 1340
McKee, C. F. 1989, ApJ, 345, 782
Miettinen, O., & Offner, S. S. R. 2013, A&A, 555, A41
Mizuno, A., Onishi, T., Yonekura, Y., et al. 1995, ApJ, 445, L161
Nagy, T., & Lendvay, G. 2017, J. Phys. Chem. Lett., 8, 4621
Narayanan, G., Heyer, M. H., Brunt, C., et al. 2008, ApJS, 177, 341
Neufeld, D. A., & Wolfire, M. G. 2017, ApJ, 845, 163
Neufeld, D. A., Goicoechea, J. R., Sonnentrucker, P., et al. 2010, A&A, 521, L10
Neufeld, D. A., Godard, B., Gerin, M., et al. 2015, A&A, 577, A49
Ohishi, M., & Kaifu, N. 1998, Faraday Discuss., 109, 205
Onishi, T., Mizuno, A., Kawamura, A., Ogawa, H., & Fukui, Y. 1996, ApJ, 465, 815
Onishi, T., Mizuno, A., Kawamura, A., Tachihara, K., & Fukui, Y. 2002, ApJ, 575, 950
Oppenheimer, M., & Dalgarno, A. 1974, ApJ, 192, 29
Pacheco-Vázquez, S., Fuente, A., Baruteau, C., et al. 2016, A&A, 589, A60
Padoan, P., Cambrésy, L., & Langer, W. 2002, ApJ, 580, L57
Padovani, M., Galli, D., & Glassgold, A. E. 2009, A&A, 501, 619
Padovani, M., Hennebelle, P., & Galli, D. 2013, A&A, 560, A114
Palumbo, M. E., Tielens, A. G. G. M., & Tokunaga, A. T. 1995, ApJ, 449, 674
Pires, W. A. D., Garrido, J. D., Nascimento, M. A. C., & Ballester, M. Y. 2014, PCCP, 16, 12793
Poglitsch, A., Waelkens, C., Geis, N., et al. 2010, A&A, 518, L2
Qu, C., & Bowman, J. M. 2016, J. Phys. Chem. A, 120, 4988
Roshi, D. A., Goss, W. M., & Jeyakumar, S. 2014, ApJ, 793, 83
Savage, B. D., & Sembach, K. R. 1996, ARA&A, 34, 279
Schnee, S., Caselli, P., Goodman, A., et al. 2007, ApJ, 671, 1839
Schnee, S., Enoch, M., Noriega-Crespo, A., et al. 2010, ApJ, 708, 127
Ungerechts, H., & Thaddeus, P. 1987, ApJS, 63, 645
van der Tak, F. F. S., Black, J. H., Schöier, F. L., Jansen, D. J., & van Dishoeck, E. F. 2007, A&A, 468, 627
Vidal, T. H. G., Loison, J.-C., Jaziri, A. Y., et al. 2017, MNRAS, 469, 435
Wilson, T. L., & Rood, R. 1994, ARA&A, 32, 191
Xu, D., Li, D., Yue, N., & Goldsmith, P. F. 2016, ApJ, 819, 22
Yang, B., Stancil, P. C., Balakrishnan, N., & Forrey, R. C. 2010, ApJ, 718, 1062
Zanchet, A., del Mazo, P., Aguado, A., et al. 2018, PCCP, 20, 5415
Zhao, B., Caselli, P., Li, Z.-Y., et al. 2016, MNRAS, 460, 2050
Zucconi, A., Walmsley, C. M., & Galli, D. 2001, A&A, 376, 650

Appendix A: New calculations of the SO + OH → SO_2 + H reaction rate

The potential energy surface (PES) of the ground electronic state of HSO_2 system have been developed by Ballester & Varandas (2005) by fitting very accurate ab initio calculations. According to this PES, the SO($^3\Sigma$) + OH($^2\Pi$) → SO_2 + H reaction is exothermic by ≈ 1.3 eV, with two deep wells, of ≈3 eV for HOSO and of ≈2 eV for HSO_2. There is a barrier between the two wells, of energy very close to the SO + OH asymptote. The HOSO is directly connected to the SO + OH with no barrier, with the attractive dipole-dipole long-range interaction.

There have been several quasi-classical trajectory (QCT) calculations of the SO + OH → SO_2 + H rate (Ballester & Varandas 2007; Ballester et al. 2010; Pires et al. 2014) finding that this reaction presents a capture-like behavior due to the dipole-dipole interaction and a very good agreement with the available experimental rates (Blitz et al. 2000; Jourdain et al. 1979; Fair & Thrush 1969). All these experimental and theoretical results were obtained at temperatures above 200 K, and in this work we extend the simulations to lower temperatures, down to 10 K, of interstellar interest.

QCT calculations have been performed at temperatures in the 10–500 K interval, using the miQCT code (Dorta-Urra et al. 2015; Zanchet et al. 2018). For each temperature batches of 50 000 trajectories were run, starting at a distance between SO and OH center-of-mass of 125 Bohr. The initial impact parameter, b, was randomly chosen between 0 and 90 Bohrs according to a b^2 distribution. The initial translational and rotational energy of the two reactants was randomly chosen according to a Boltzmann distribution, while the vibrations of the two reactants was described using a adiabatic switching method (Grozdanov & Solov'ev 1982; Johnson 1987; Qu & Bowman 2016; Nagy & Lendvay 2017) corresponding to the ground vibrational state of the two reagents. The reactivity of this reaction does not depend on the initial vibrational excitation of the reactants (Ballester & Varandas 2007; Ballester et al. 2010; Pires et al. 2014). For this reason, we can consider that the vibrational state selected rate calculated here is essentially the thermal rate constant. The reactive rate constant is calculated as

$$k_{vj}(T) = g_e(T) \sqrt{\frac{8k_B T}{\pi\mu}} \frac{N_r}{N_t} \pi b_{\max}^2, \tag{A.1}$$

where N_r denotes the number of reactive trajectories and $b_{\max}$ is the maximum impact parameter for which reaction takes place.

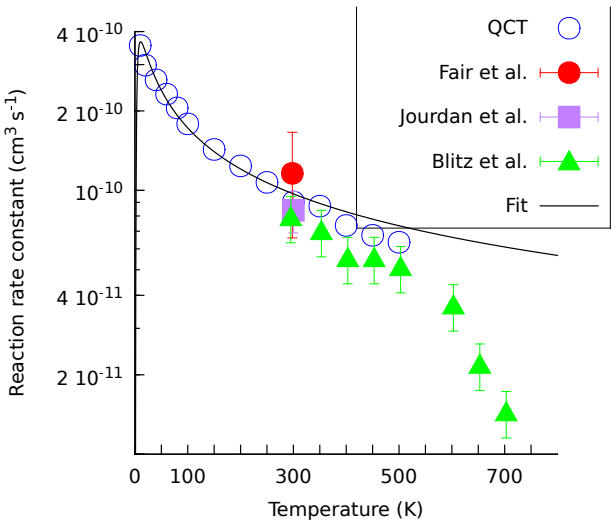

Fig. A.1. State-selected reaction rates for SO(v = 0) + OH(v = 0) → SO_2 + H collisions as a function of temperature obtained in this work (QCT), and compared with the experimental results of previous works (Blitz et al. 2000; Jourdain et al. 1979; Fair & Thrush 1969). The calculated rate has been fitted to the expression $K(T) = a(T/300)^b e^{-c/T}$, with $a = 1.24211 \times 10^{-10}$ cm^3 s^{-1} $b = -0.56049$ and $c = 6.58356$ K. This expression is adequate in the 10–300 K interval.

Finally, g_e is the electronic partition function

$$g_e(T) = \left\{3\left(1 + e^{-209/T}\right)\right\}^{-1}, \tag{A.2}$$

where the factor 3 arises because only one combination of total spin 1/2 is reactive, when combining the triplet state of SO and the double state of OH, and that the OH($^2\Pi$) splits into two spin–orbit states ($^2\Pi_{3/2}$ and $^2\Pi_{1/2}$, with an energy difference of 209 K. The results obtained are shown in Fig. A.1 and compared with the experimental results available.

The QCT results made in this work are in rather good agreement with the experimental data in the interval 300–500 K. The rate increases by a factor of 3–4 when decreasing the temperature from 300 to 10 K. This may have some consequences in astrophysical objects at low temperatures. It should be noted that the fit presented in the caption of Fig. A.1 is only adequate for temperatures between 10 and 300 K.

Appendix B: Additional tables and figures

Table B.1. Telescope parameters.

Telescope	Setup	Freq. band	*HPBW* (″)	$F_{\rm eff}$	$B_{\rm eff}$
IRAM 30 m	Setup 1	L106	24	0.95	0.80
	Setup 2	L89	29	0.95	0.81
		L147	16	0.93	0.74
	Setup 3	L101	25	0.95	0.80
		L138	17	0.93	0.74
	Setup 4	L92	27	0.95	0.81
		L168	14	0.93	0.74
Yebes 40 m	Setup 0	L23000	84	0.93	0.70
		L44750	42	0.90	0.49

Table B.2. Spectral setups.

	Line	Freq. (MHz)	E_u (K)	A_{ul} (s^{-1})	g_u
		L89			
HCS^+	$2 \rightarrow 1$	85 347.87	6.1	1.110×10^{-5}	5
HCN	$1 \rightarrow 0$	88 631.85	4.3	2.406×10^{-5}	3
$H^{13}CN$	$1 \rightarrow 0$	86 340.18	4.1	2.224×10^{-5}	3
$HC^{15}N$	$1 \rightarrow 0$	86 054.97	4.1	2.202×10^{-5}	3
HCO^+	$1 \rightarrow 0$	89 188.53	4.3	4.234×10^{-5}	3
$H^{13}CO^+$	$1 \rightarrow 0$	86 754.29	4.2	3.897×10^{-5}	3
$HC^{18}O^+$	$1 \rightarrow 0$	85 162.22	4.1	3.686×10^{-5}	3
HNC	$1 \rightarrow 0$	90 663.56	4.4	2.690×10^{-5}	3
OCS	$7 \rightarrow 6$	85 139.10	16.3	1.715×10^{-6}	15
SO	$2_2 \rightarrow 1_1$	86 093.96	19.3	5.250×10^{-6}	5
		L92			
^{13}CS	$2 \rightarrow 1$	92 494.27	6.7	1.412×10^{-5}	5
$C^{34}S$	$2 \rightarrow 1$	96 412.95	6.9	1.600×10^{-5}	5
CH_3OH	$2,-1 \rightarrow 1,-1$	96 739.36	4.6	2.558×10^{-5}	5
CH_3OH	$2,1 \rightarrow 1,1$	96 741.37	7.0	3.408×10^{-6}	5
		L101			
CS	$2 \rightarrow 1$	97 980.95	7.1	1.679×10^{-5}	5
SO	$2_3 \rightarrow 1_2$	99 299.89	9.2	1.125×10^{-5}	7
^{34}SO	$2_3 \rightarrow 1_2$	97 715.40	9.1	1.073×10^{-5}	7
H_2CS	$3(1,2) \rightarrow 2(1,2)$	101 477.81	8.1	1.260×10^{-5}	7
		L106			
^{13}CO	$1 \rightarrow 0$	110 201.35	5.3	6.336×10^{-8}	3
$C^{18}O$	$1 \rightarrow 0$	109 782.17	5.3	6.263×10^{-8}	3
N_2H^+	$1 \rightarrow 0$	93 173.77	4.5	3.628×10^{-5}	3
SO	$3_2 \rightarrow 2_1$	109 252.18	21.1	1.080×10^{-5}	5
^{34}SO	$3_2 \rightarrow 2_1$	106 743.37	20.9	1.007×10^{-5}	5
NH_2D	$1(1,1) \rightarrow 1(0,1)$	110 153.59	21.3	5.501×10^{-6}	9
CH_3OH	$0,0 \rightarrow 1,-1$	108 893.94	5.2	1.471×10^{-5}	3
		L138			
^{13}CS	$3 \rightarrow 2$	138 739.26	13.3	5.107×10^{-5}	7
SO	$3_4 \rightarrow 2_3$	138 178.66	15.9	3.166×10^{-5}	9
OCS	$11 \rightarrow 10$	133 785.90	38.5	6.818×10^{-6}	23
H_2CS	$4(0,4) \rightarrow 3(0,3)$	137 371.21	16.5	3.647×10^{-5}	9
HDCO	$2(1,1) \rightarrow 1(1,0)$	134 284.90	17.6	4.591×10^{-5}	5
		L147			
CS	$3 \rightarrow 2$	146 969.03	14.1	6.071×10^{-5}	7
$C^{34}S$	$3 \rightarrow 2$	144 617.10	13.9	5.784×10^{-5}	7
		L168			
H_2S	$1(1,0) \rightarrow 1(0,1)$	168 762.75	8.1	2.677×10^{-5}	3
$H_2{}^{34}S$	$1(1,0) \rightarrow 1(0,1)$	167 910.52	8.1	2.616×10^{-5}	3
HCS^+	$4 \rightarrow 3$	170 691.62	20.5	9.863×10^{-5}	9
$HC^{34}S^+$	$4 \rightarrow 3$	167 927.25	20.1	7.805×10^{-5}	9
SO	$4_4 \rightarrow 3_3$	172 181.42	33.8	5.833×10^{-5}	9
^{34}SO	$4_4 \rightarrow 3_3$	168 815.11	33.4	5.498×10^{-5}	9
		L23000			
NH_3	$(1,1)a \rightarrow (1,1)s$	23 694.49	1.1	1.712×10^{-7}	12
NH_3	$(2,2)a \rightarrow (2,2)s$	23 722.63	42.3	2.291×10^{-7}	20
		L44500			
CS	$1 \rightarrow 0$	48 990.96	2.4	1.749×10^{-6}	3
$C^{34}S$	$1 \rightarrow 0$	48 206.94	2.3	1.666×10^{-6}	3
^{13}CS	$1 \rightarrow 0$	46 247.56	2.2	1.471×10^{-6}	3
HCS^+	$1 \rightarrow 0$	42 674.19	2.0	1.156×10^{-6}	3
OCS	$4 \rightarrow 3$	48 651.60	5.8	3.047×10^{-7}	9

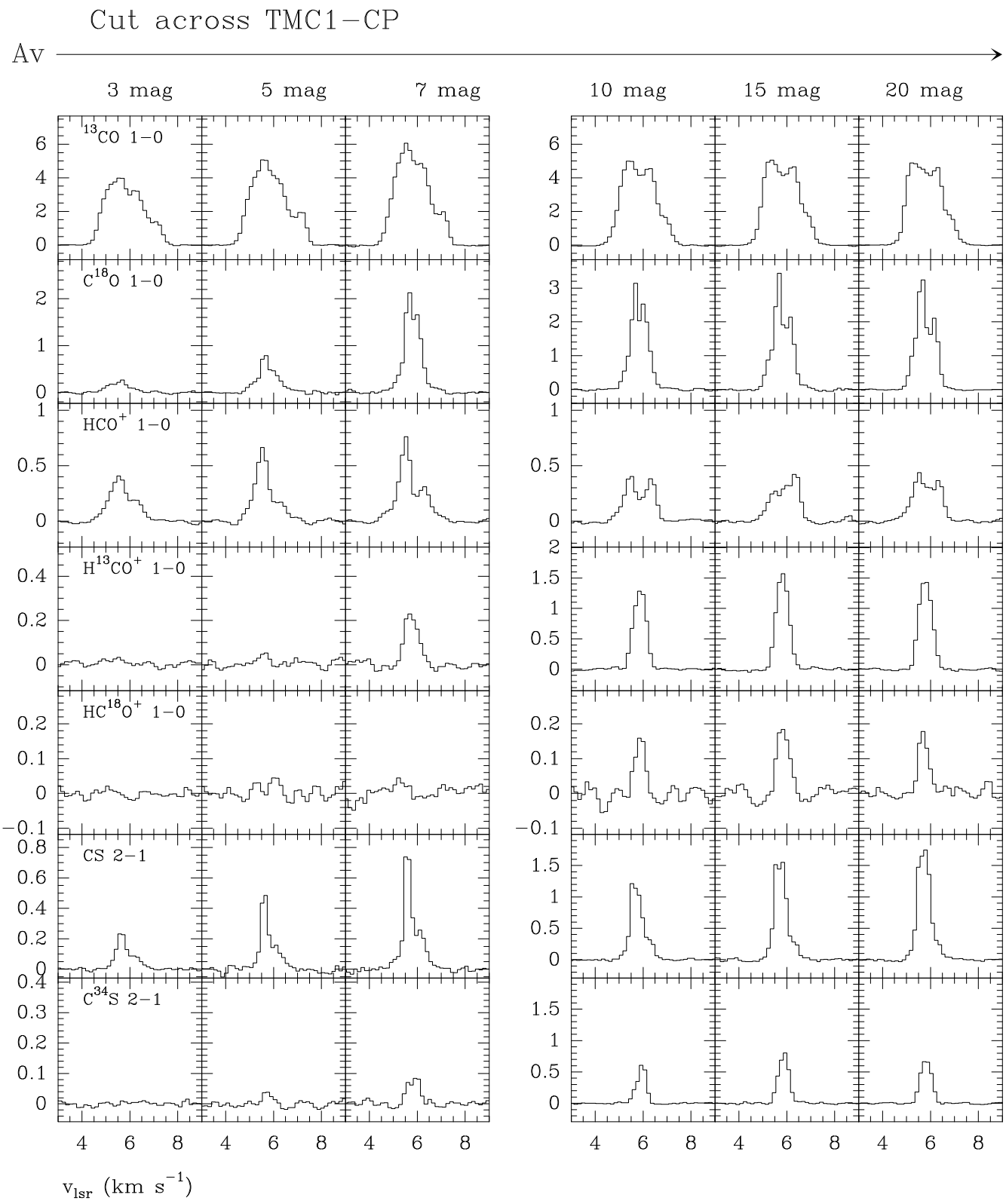

Fig. B.1. Selected sample of spectra as observed with the 30 m telescope towards the TMC 1-CP cut (in T_{MB}).

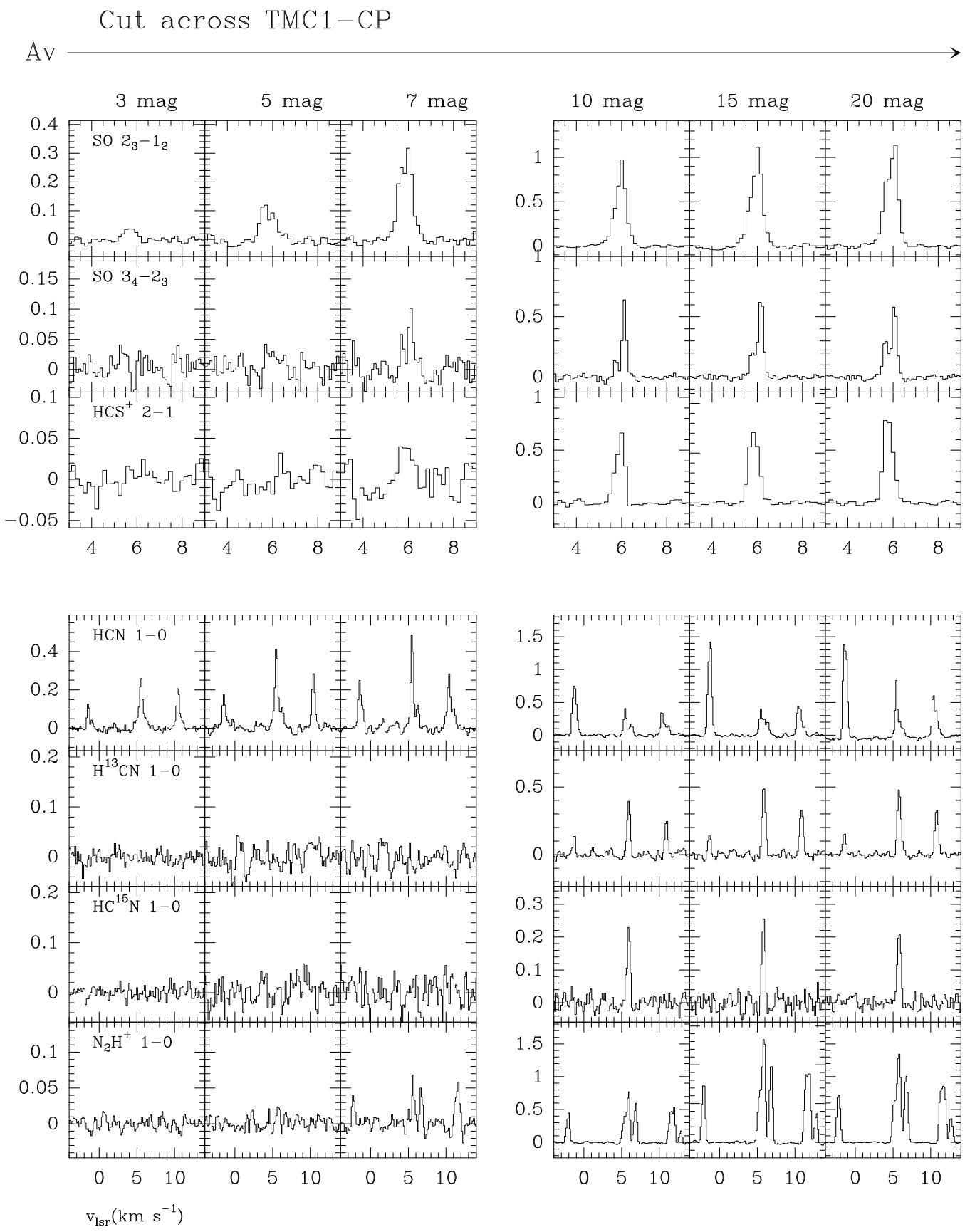

Fig. B.1. continued.

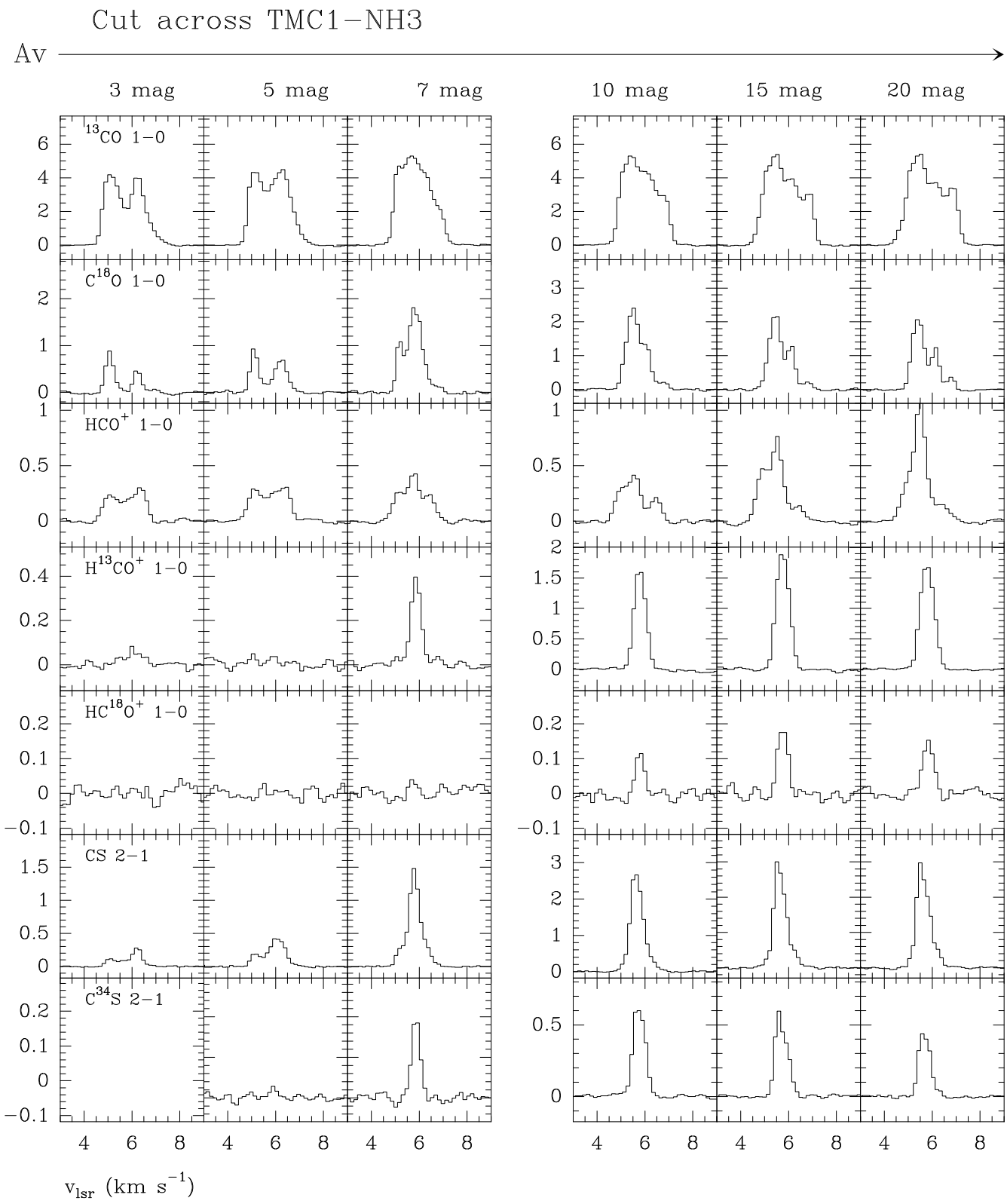

Fig. B.2. Selected sample of spectra as observed with the 30 m telescope towards the TMC 1-NH3 cut (in T_{MB}).

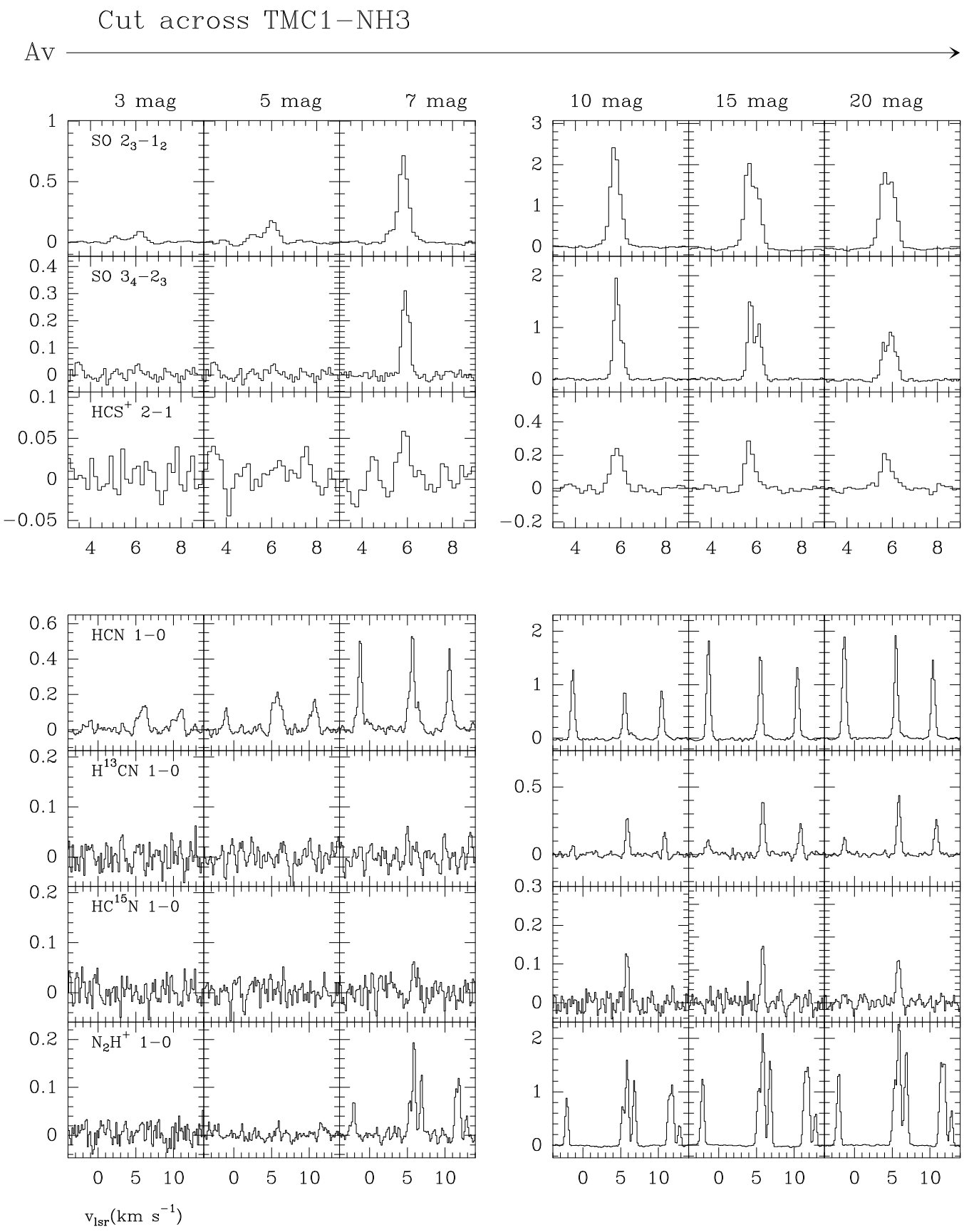

Fig. B.2. continued.

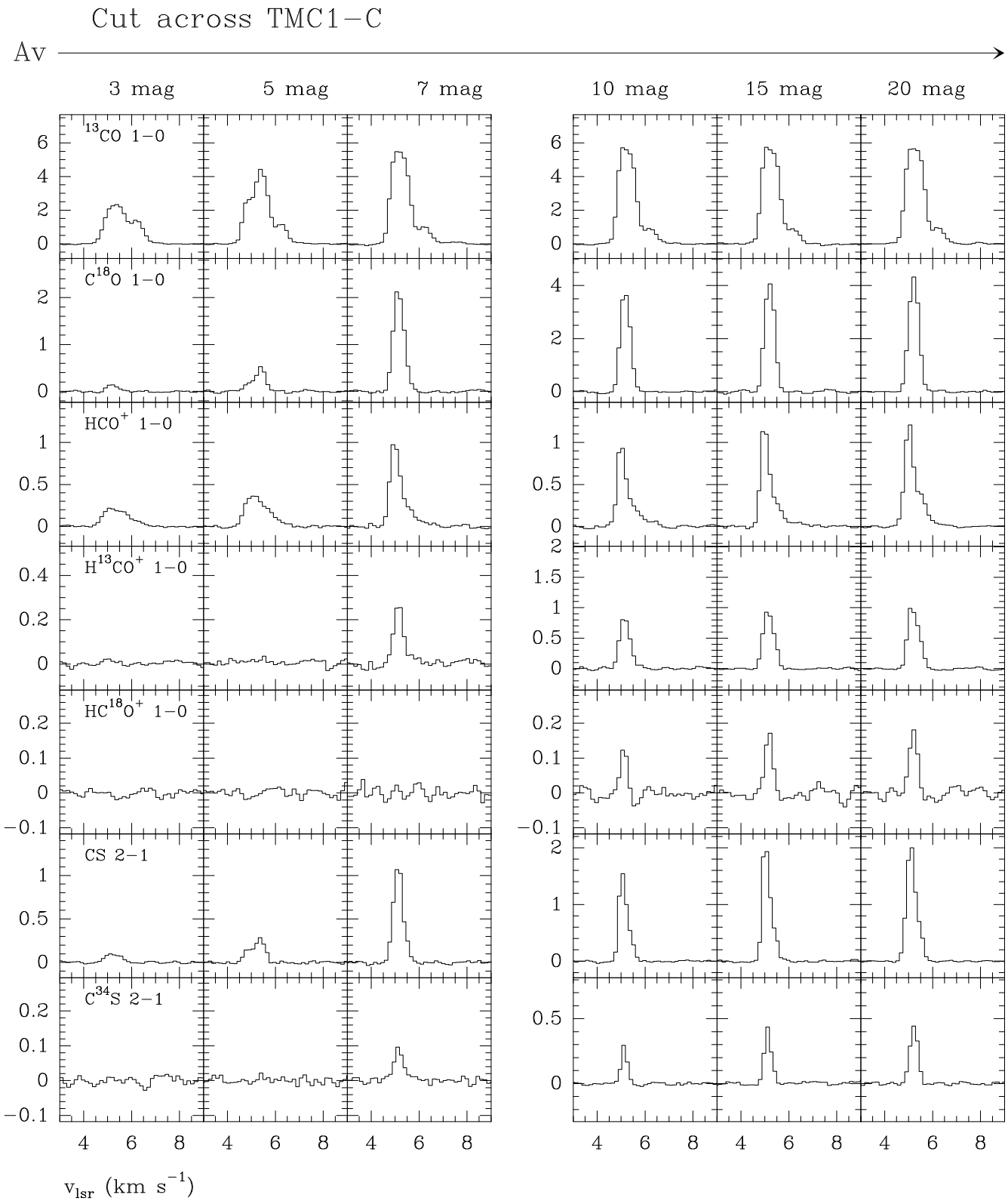

Fig. B.3. Selected sample of spectra as observed with the 30 m telescope towards the TMC 1-C cut (in T_{MB}).

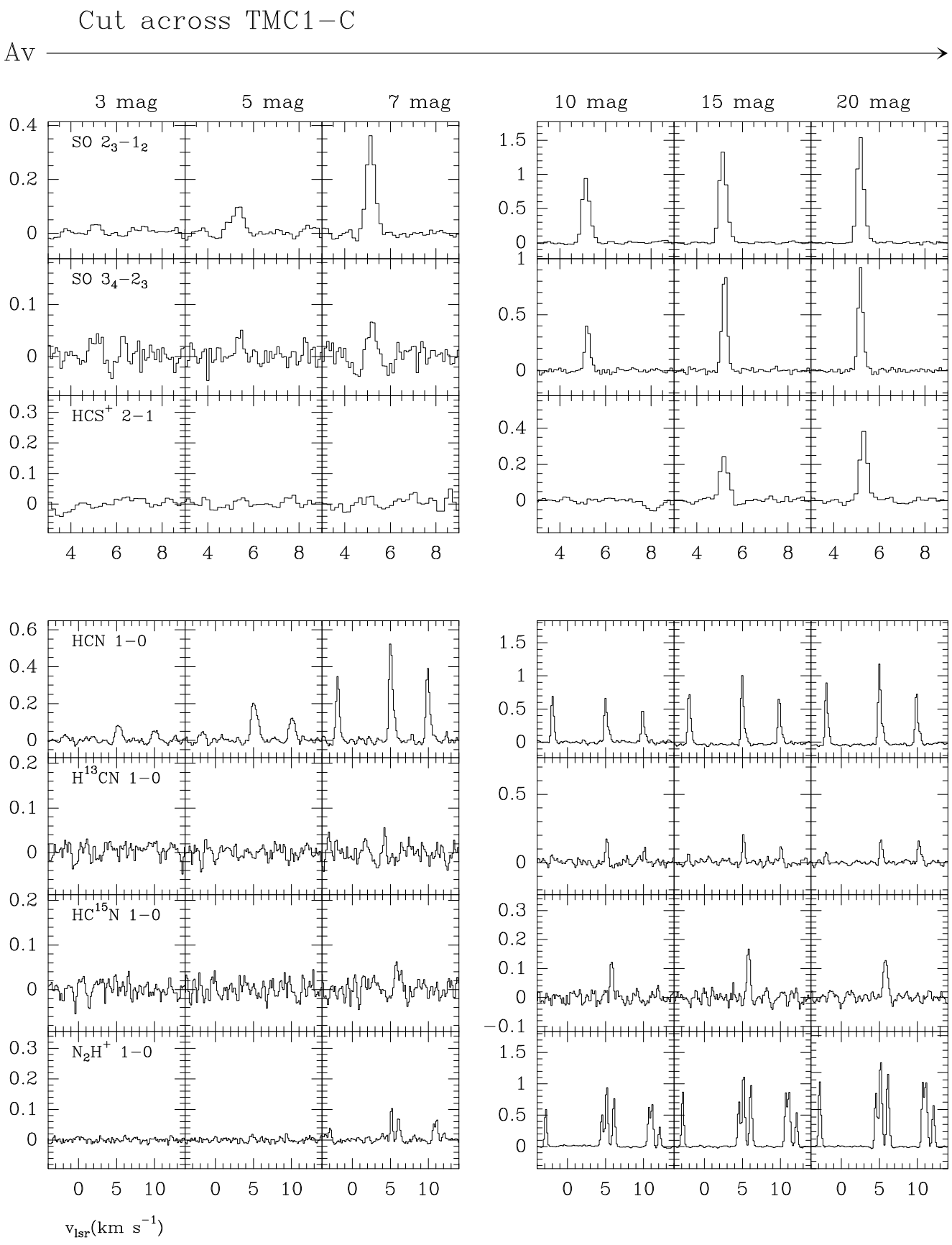

Fig. B.3. continued.